

Contents lists available at [ScienceDirect](https://www.sciencedirect.com)

Journal of Sound and Vibration

journal homepage: www.elsevier.com/locate/jsv

Nonlinear broadband time-domain admittance boundary condition for duct acoustics. Application to perforated plate liners

Daher Diab*, Didier Dragna, Edouard Salze, Marie-Annick Galland

Univ Lyon, Ecole Centrale de Lyon, CNRS, Univ Claude Bernard Lyon 1, INSA Lyon, LMFA, UMR5509, 69130, Ecully, France

ARTICLE INFO

Keywords:

Nonlinear admittance
Perforated plate
Time-domain simulation
Time-domain admittance boundary condition
Spatially-varying admittance

ABSTRACT

The behavior of perforated plates at high excitation level is generally modeled by a surface impedance that depends on the rms velocity in the perforations. A time-domain admittance boundary condition (TDABC) is developed to account for this variation using a multipole model. Two formulations are considered, based on the interpolation either of the admittance or of the multipole coefficients from a data set of reference values. These TDABC are implemented in a finite-difference time-domain solver of the linearized Euler equations and are validated by comparison with experimental results on an impedance tube. Application to a two-dimensional lined duct corresponding to the reference geometry of the NASA Grazing Incidence Tube is then performed. The spatial variation of the perforated plate liner impedance is highlighted and it is shown that assuming a uniform impedance can lead to an unacceptable prediction of the liner attenuation. These results are confirmed both for a harmonic or broadband excitation.

1. Introduction

Acoustic liners are widely used for noise reduction in several industrial applications such as nacelles of aircraft engines, exhaust ducts or air ventilation systems. Among them, the perforated plate (PP) liner is probably the most employed, because of its simplicity, its efficiency and its applicability to extreme environmental conditions (temperature and pressure) where porous materials cannot be used. It is made of a perforated plate, mounted on a honeycomb cavity attached to the system frame. This liner behaves as a resonator. As such, PP liners provide a significant acoustic attenuation, but only near the resonant frequencies that depend mainly on the cavity depth.

Starting from Sivian [1], it has been noted that the perforated plate excited by an acoustic wave with a large amplitude exhibits a nonlinear behavior. More precisely, the measured acoustic impedance was shown to depend on the rms velocity in the perforation. This behavior is associated to the flow separation that occurs at the perforation edges for a sufficiently large amplitude of the velocity in the perforation. This induces generation of vortices and conversion of acoustic energy into vortical energy, which results in an increase of the plate resistance. Even for moderate SPL (around 110–120 dB), at which sound propagation remains a linear process, perforated plates can exhibit a nonlinear behavior. In ducted systems, such as engine nacelles, the sound pressure level (SPL) can be much higher. In such conditions, the nonlinear response of PP liners must be accounted for.

Detailed direct numerical simulations of the flow in a perforated liner excited by an acoustic wave with a large amplitude have been already performed [2,3]. Due to their high computational cost, they are however limited to simple configurations. For predicting the sound attenuation brought by a whole panel, it is more suitable to rely on numerical simulations in which the acoustic behavior of the perforated liner is modeled.

* Corresponding author.

E-mail addresses: daher.diab@ec-lyon.fr (D. Diab), didier.dragna@ec-lyon.fr (D. Dragna), edouard.salze@ec-lyon.fr (E. Salze), marie-annick.galland@ec-lyon.fr (M.-A. Galland).

<https://doi.org/10.1016/j.jsv.2022.116892>

Received 30 August 2021; Received in revised form 16 February 2022; Accepted 6 March 2022

Available online 14 March 2022

0022-460X/© 2022 Elsevier Ltd. All rights reserved.

To do so, the most common approach is to employ a surface impedance model of the perforated plate liner, that includes nonlinear effects. It should be noted that the concept of surface impedance is strictly valid in the linear regime. It can be extended for a sinusoidal excitation in the nonlinear regime without difficulty, as long as the harmonic distortion remains limited. In the other cases, especially for a broadband excitation, the surface impedance in the nonlinear regime has to be used carefully. Several semi-empirical models for surface impedance of perforated plate liners [4–9] have been proposed. In most of them, based on measurements reported in the literature (among others Refs. [10,11]), the nonlinear correction consists in an increase of the resistance and a decrease of the orifice end correction, with the amplitude of the acoustic velocity in the orifice. Recently, Laly et al. [12] have extended in the nonlinear regime the model developed by Atalla and Sgard [13] based on an equivalent fluid approach to represent perforated panels: the resistivity and the tortuosity of the equivalent fluid depends on the geometrical properties of the perforated plate as well as the amplitude of the acoustic velocity in the perforation. An other approach proposed by Cummings [14] is to directly relate the pressure jump at the perforated plate and the velocity in the perforation through a nonlinear differential equation in the time-domain.

Nevertheless, there are few attempts to account for nonlinear models of PP liners in numerical simulations of sound propagation in lined ducts. One can refer to Eversman [15] or, more recently, to Roncen et al. [16], that use frequency-domain approaches to investigate the effect of nonlinearity on liner performance in a flow duct. While frequency-domain methods can still be used for a high-level harmonic excitation, time-domain methods are the natural approach to account for nonlinear effects. In the time-domain, the impedance boundary condition translates into a convolution, whose direct numerical evaluation is time-consuming [17]. A vast literature thus aimed at proposing time-domain impedance or admittance boundary conditions (TDIBC or TDABC) in the linear regime (e.g. [17–21]). Among the proposed approaches, TDIBC based on the multipole model has attracted lot of attention [19,22–24], as it can be used to represent surface impedance models of generic liners and as it allows for an efficient numerical implementation. In particular, Dragna et al. [25] and Troian et al. [24] proposed the auxiliary differential equation (ADE) method, in which the calculation of the convolution is reduced to the time integration of additional first-order partial differential equations. This is especially well-suited for high-order methods. Recently, Shur et al. [26] extended this TDIBC based on the multipole model in the nonlinear regime.

The objectives of the paper are to propose and evaluate formulations of the TDABC for the multipole model in the nonlinear regime and to exemplify sound propagation along a lined duct in high sound pressure environment. The impedance model proposed by Laly et al. [12] is used as the reference model for the perforated panel. Two approaches for the TDABC in the nonlinear regime are considered. In the first one, based on Shur et al. [26], the admittance is interpolated as a function of the rms velocity in the orifice. In the second one, the poles and coefficients of the multipole model are directly interpolated as a function of the rms velocity in the orifice. The two approaches are validated against a one-dimensional (1D) impedance tube configuration, first for numerical experiments and then for measurements performed for three perforated plates. Application to a two-dimensional (2D) lined duct is then performed. The evolution of the liner attenuation with the excitation level is studied. The spatial variation of the surface impedance along the liner is analyzed. Finally, it is investigated whether or not accounting for the spatial variations of the impedance is important for accurately predicting the liner attenuation.

This paper is organized as follows. Section 2 presents the acoustic impedance model of Laly et al. [12] for predicting the response of perforated panels at high level of excitation. In Section 3, the numerical model that solves the linearized Euler equations in the time-domain using finite difference techniques is described. The time domain admittance boundary condition based on the multipole model is first presented in the linear regime. The two extensions of the TDABC in the nonlinear regime are then introduced. The validation of the proposed approach is performed in Section 4. Application to a 2D lined duct is then investigated in Section 5. Concluding remarks are finally given in Section 6.

2. Impedance model of perforated plates in the nonlinear regime

Throughout the paper, the time-dependence convention $e^{-j\omega t}$ is used, where ω denotes the angular frequency, j the imaginary complex number ($j^2 = -1$) and t the time. The air is characterized by its density ($\rho_0 = 1.211 \text{ kg m}^{-3}$), its dynamic viscosity ($\eta = 1.84 \times 10^{-5} \text{ kg m}^{-1} \text{ s}^{-1}$) and the corresponding sound speed ($c_0 = 340 \text{ m s}^{-1}$). The geometry of the perforated plate is described by its thickness h , the perforation radius r and the percentage open area (POA) φ .

Atalla and Sgard [13] modeled the perforated panel in the linear regime by an equivalent fluid model following the Johnson-Allard approach [27]. The normalized acoustic impedance of a perforated panel backed by an air cavity of depth D is

$$Z_L = \frac{-j\omega\alpha_\infty h}{c_0\varphi} \left(1 - \frac{\sigma\varphi}{j\omega\rho_0\alpha_\infty} \sqrt{1 - \frac{4j\omega\rho_0\eta\alpha_\infty^2}{\varphi^2\sigma^2\Lambda^2}} \right) - \coth(jk_0D), \quad (1)$$

where $k_0 = \omega/c_0$ is the wave number in air. The parameters of the equivalent fluid are related to the PP geometry. Thus, the viscous characteristic length Λ is equal to the perforation radius ($\Lambda = r$). The flow resistivity σ is given by $\sigma = \frac{8\eta}{\varphi r^2}$ in the case of cylindrical orifices. The tortuosity α_∞ is a function of the correction length ε , that accounts for sound radiation effects at the end of the perforations through $\alpha_\infty = 1 + \frac{2\varepsilon}{h}$. The correction length is related to the POA and the radius of perforation. Following Laly et al. [12], it can be written:

$$\varepsilon = \Psi 0.48 \sqrt{\pi r^2} \left[\sum_{n=0}^8 a_n (\sqrt{\varphi})^n \right], \quad (2)$$

Table 1
Geometric parameters of the PPs absorber.

	PP#1	PP#2	PP#3
Plate thickness (mm)	1	1	1
Perforation radius (mm)	0.25	0.25	1
Perforation ratio (%)	1.5	1	1.5

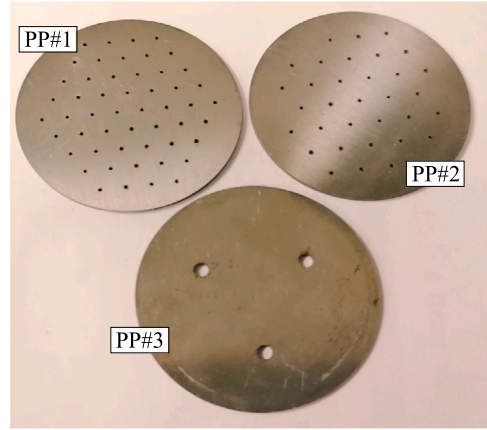


Fig. 1. Photo of the three perforated plates considered.

where $0.48\sqrt{\pi r^2}$ is the correction length for a single circular orifice, the sum over the coefficients a_n is an approximation of the Fok function that accounts for orifice interaction effects [11] and Ψ is a constant. The coefficients a_n are given by $a_0 = 1$, $a_1 = -1.4092$, $a_2 = 0$, $a_3 = 0.33818$, $a_4 = 0$, $a_5 = 0.06793$, $a_6 = -0.02287$, $a_7 = 0.003015$ and $a_8 = -0.01614$ [11] and Ψ is set to $4/3$. Note that the Fok function and the empirical constant Ψ are not present in the original model proposed by Atalla and Sgard [13], but are introduced here for coherence with the nonlinear model.

Laly et al. [12] proposed an extension of the model in Eq. (1) to characterize the acoustic response of perforated plates in the nonlinear regime. The impedance model of a PP backed by an air layer has the same form as in the linear regime:

$$Z_{NL} = \frac{-j\omega h}{c_0\varphi} \alpha_{\infty NL} \left(1 - \frac{\sigma_{NL}\varphi}{j\omega\rho_0\alpha_{\infty NL}} \sqrt{1 - \frac{4j\omega\rho_0\eta\alpha_{\infty NL}^2}{\varphi^2\sigma_{NL}^2\Lambda^2}} \right) - \coth(jk_0 D), \quad (3)$$

except that the flow resistivity σ_{NL} and the tortuosity $\alpha_{\infty NL}$ now depend on the rms velocity in the orifice v_{rms} . The flow resistivity of the PP in the nonlinear regime is modeled via a Forchheimer-type law. It is thus equal to its value in the linear regime plus a nonlinear correction:

$$\sigma_{NL} = \sigma + \frac{\beta\rho_0(1-\varphi^2)}{\pi h\varphi C_D^2} \sqrt{2}v_{rms}, \quad (4)$$

where C_D is the discharge coefficient, that depends on the perforation geometry, the edge sharpness among others and that vary between 0.6 and 0.8 and β is a coefficient. Thereafter, the values used in Laly et al. [12], i.e. $C_D = 0.76$ and $\beta = 1.6$, are employed. The tortuosity $\alpha_{\infty NL}$ in the nonlinear regime is defined as in the linear regime by

$$\alpha_{\infty NL} = 1 + \frac{2\varepsilon_{NL}}{h}. \quad (5)$$

Following Maa [5], the correction length ε_{NL} is modified to account for the nonlinear effects with

$$\varepsilon_{NL} = \varepsilon \left(1 + \frac{\sqrt{2}v_{rms}}{\varphi c_0} \right)^{-1}. \quad (6)$$

The tortuosity thus decreases with the increase of the acoustic velocity in the perforation.

The model proposed by Laly et al. [12] is more accurate for micro-perforated liners ($r \leq 0.5$ mm) than for macro-perforated liners and for a POA range from 1% to 5% [28].

In this work, results are exemplified for three PP absorbers, whose photo is shown in Fig. 1. Their geometrical characteristics are given in Table 1. The PPs #1 and #2 correspond to micro-perforated plates, with perforation radius below 0.5 mm and POA in the order of 1%. PP#3 has a larger perforation radius and is in between a micro- and macro-perforated plate.

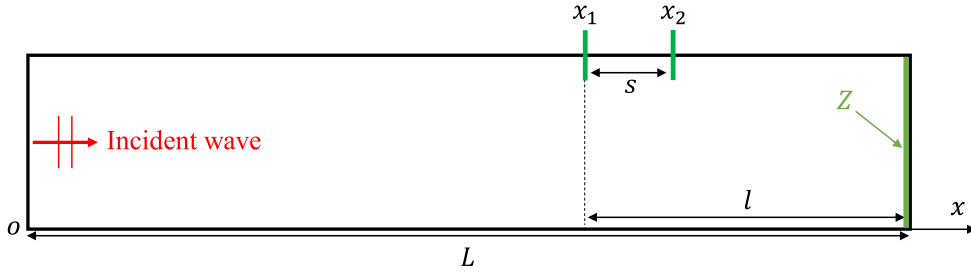


Fig. 2. Schematic for the one-dimensional configuration, corresponding to an impedance tube.

3. Time-domain numerical model

3.1. Geometrical configuration

An impedance tube, schematized in Fig. 2, is considered as a canonical problem to evaluate time-domain impedance boundary conditions in the nonlinear regime. It is treated as a one-dimensional problem. Denoting by x the spatial variable, the domain of interest is limited to $0 \leq x \leq L$. The PP liner is located at $x = L$ and an incident wave $p_i(t)$ is traveling towards the liner.

3.2. Equations and numerical methods

For acoustic perturbations of sufficiently small amplitude, sound propagation is governed by the linearized Euler equations (LEE). For a homogeneous medium at rest, they write:

$$\begin{cases} \frac{\partial u}{\partial t} + \frac{1}{\rho_0} \frac{\partial p}{\partial x} = 0 \\ \frac{\partial p}{\partial t} + \rho_0 c_0^2 \frac{\partial u}{\partial x} = 0, \end{cases} \quad (7)$$

where u and p are the acoustic velocity and pressure, respectively.

The LEE are solved using high-order finite-difference time-domain methods. The spatial derivatives are calculated using optimized 4th-order finite differences schemes over 11 points [29,30]. Time integration is performed using an optimized 6-stage 4th-order Runge–Kutta algorithm [31]. In order to avoid numerical instabilities and to remove grid-to-grid oscillations, optimized selective filters [30,32] are applied after each time iteration.

The incident wave $p_i(t)$ is prescribed using the method of characteristics. The incoming and outgoing characteristics in the computational domain at the boundary $x = 0$, denoted by q_i and q_o , respectively, are given by:

$$q_i(t) = \frac{1}{2}(p(x=0, t) + Z_0 u(x=0, t)) \quad q_o(t) = \frac{1}{2}(p(x=0, t) - Z_0 u(x=0, t)), \quad (8)$$

with $Z_0 = \rho_0 c_0$. To force the incident wave and avoid reflections at the boundary, the method consists in determining the outgoing characteristic from the numerical solution and imposing the incoming characteristic to $q_i(t) = p_i(t)$, after each stage of the Runge–Kutta algorithm. The pressure and the velocity at the boundary are then corrected with the relations:

$$p(x=0, t) = q_i(t) + q_o(t) \quad u(x=0, t) = \frac{q_i(t) - q_o(t)}{Z_0} \quad (9)$$

Finally, all variables are initialized to zero at time $t = 0$.

3.3. Time-domain admittance boundary condition (TDABC) in the linear regime

Before discussing its extension for the nonlinear regime, the time-domain admittance boundary condition proposed by Troian et al. [24] for the linear regime is briefly summarized. Implementation on the admittance rather than on the impedance was preferred, as numerical instabilities were observed for some liners in the latter case. Note that implementations based on the reflection coefficient have been also proposed [19] and seem to offer better stability properties [33]. Denoting by $Y(\omega)$ the normalized surface admittance, the admittance boundary condition is defined in the frequency domain by $Z_0 U_n(\omega) = Y(\omega) P(\omega)$, with $U_n = \mathbf{U} \cdot \mathbf{n}$ where $P(\omega)$ and $\mathbf{U}(\omega)$ are the Fourier transforms of the acoustic pressure and velocity on the PP surface, respectively, and \mathbf{n} is the normal unit vector pointing into the liner surface.

The time domain admittance boundary condition (TDABC) is obtained from the translation of the frequency domain boundary condition, yielding the convolution $Z_0 u_n(t) = [y * p](t)$, where $y(t)$ is the surface admittance in the time domain. To avoid the tedious

calculation of the convolution integral, Troian et al. [24] proposed to express the broadband admittance model $Y(\omega)$ as a multipole model:

$$Y(\omega) = Y_\infty + \sum_{k=1}^P \frac{A_k}{\lambda_k - j\omega}, \quad (10)$$

where λ_k are the poles of the admittance and P denotes their number. Note that the poles and the associated coefficients A_k are either real or come as complex conjugate pairs. Finally, the coefficient Y_∞ is real-valued.

The analytical surface admittance of the PP is obtained from Eq. (1) with $Y(\omega) = [Z_L(\omega)]^{-1}$ and is approximated by a multipole model in the form of Eq. (10). To do so, the poles and the coefficients of the broadband admittance are determined using the vector fitting (VF) algorithm [34] in the frequency band of interest. The VF algorithm allows the multipole model to have stable poles. The passivity of the multipole model ($\text{Re}[Y(\omega)] \geq 0$ for $\omega > 0$) is however not guaranteed and has to be checked for all frequencies and for each set of coefficients obtained with the VF algorithm. In particular, it was observed that the real part of the multipole model can be negative at very low frequencies for PP liners. Generally, this issue can be overcome by increasing the number of poles. This solution might however not be worthwhile because we usually want to keep the number of poles as small as possible to reduce the computational cost. As the minimum of $\text{Re}[Y]$ denoted by Y_- generally remains small (Y_- in the order of -10^{-3}), an alternative to enforce passivity is to add $-Y_-$ to Y_∞ so that $\text{Re}[Y] \geq 0$ over the frequency band of interest.

With the multipole form, the surface admittance in the time domain has a closed-form expression, that greatly simplifies the expression of the convolution. After some calculation detailed in Ref. [24], the time-domain admittance boundary condition (TDABC) finally relates the acoustic velocity and pressure on the liner surface with the expression:

$$Z_0 u_n(t) = Y_\infty p(t) + \sum_{k=1}^P A_k \phi_k(t), \quad (11)$$

where the new temporal functions $\phi_k(t)$, called accumulator in Reymen et al. [22], verify the system of ordinary differential equations (ODE):

$$\frac{d\phi_k}{dt} + \lambda_k \phi_k(t) = p(t) \quad (12)$$

This system is numerically solved using the same time scheme as for the LEE presented in Eq. (7). Eqs. (11) and (12) constitute the TDABC.

Note that the formulation of the TDABC presented in this section is an alternative to that proposed in Ref. [24], as there is no explicit distinction between the real poles and the pairs of complex conjugate poles. As a consequence, the accumulators ϕ_k are complex-valued.

3.4. Extension of the TDABC in the nonlinear regime

Some remarks are first made on nonlinear impedance models. Surface impedance is rigorously defined in the linear regime. For a harmonic excitation, a surface impedance that depends on the excitation amplitude seems relevant, as long as the harmonic distortion is negligible. For other types of excitation, the concept of nonlinear surface impedance is somewhat empirical. A straightforward extension of the impedance model proposed by Laly et al. [12] for broadband stationary signal is to consider that the main information on the velocity in the perforations governing the nonlinear effects remains its overall amplitude rather than any specific frequency-dependent information. Such approach has been employed by Eversman [15] for propagation of multiple tones inside a lined duct using a frequency-domain finite element method. Therefore, the impedance model in Eq. (3) can be used as is for a broadband stationary excitation.¹ Despite its simplicity, recent comparisons [35] have shown an excellent agreement between predictions using this approach and measurements with an impedance tube for a white noise excitation.

The rest of the study is thus limited to stationary signals. For non-stationary signals, such as transient signals, other models than frequency-based surface impedance models might be better suited to represent the acoustic response of perforated plates in the nonlinear regime. Thus, Cummings [14] propose nonlinear differential equations in the time-domain, that directly relate the velocity in the perforation and the pressure jump through the perforated plate. These equations are obtained from simplification of the fluid mechanics equations and do not include all physical effects considered in the surface impedance model, such as the effects of the interaction between holes of the perforates on the end correction length or the reduction of the end correction length with the increase of the orifice velocity. Comparisons were however performed for a transmitted pulse through a perforated plate between measurements in an impedance tube and numerical predictions and were promising. Implementation of such nonlinear models of perforated plates for time-domain simulations in a lined duct has been done in Monteghetti et al. [33].

The implementation of the nonlinear TDABC in the time-domain numerical model is now presented. It is based on the recent work of Shur et al. [26] that has extended the TDABC of Troian et al. [24] in the nonlinear regime. To do so, a quasi-steady approach is employed. The idea is that the rms velocity on the liner has to be determined from the numerical solution. As the solution is however advanced in time starting from some initial conditions, a transient period is necessarily present. Thus, a time-varying evaluation of v_{rms} , denoted by $\bar{v}_{\text{rms}}(t)$, is determined and the surface admittance is dynamically modified to $Y(\omega, \bar{v}_{\text{rms}})$, until steady-state is reached.

¹ Other nonlinear surface impedance models are based on the rms acoustic pressure on the liner rather than the rms velocity in the perforations, as considered by Shur et al. [26]. The numerical methods presented subsequently can be also employed similarly.

Second, to account for the variation of the admittance with both ω and v_{rms} , two approaches are investigated. They are both based on the approximation of the admittance by a multipole model for some reference values of v_{rms} , that allows for the use of the ADE method. In the first approach proposed by Shur et al. [26], the admittance is determined for a given v_{rms} by interpolation. This method was shown to be accurate and efficient. One of its drawback is that compared to the linear regime, the number of poles significantly increases and is globally proportional to the number of reference values of v_{rms} chosen for the interpolation. This first approach, referred to as the interpolation of the admittance (IA) method is detailed in Section 3.4.1. We propose a second approach, in which, the multipole coefficients, rather than directly the admittance, are calculated for a given v_{rms} by interpolation. Once the coefficients are known, the admittance is easily deduced. This approach, referred to as the interpolation of the admittance parameters (IAP) method is presented in Section 3.4.2.

3.4.1. Interpolation of the admittance (IA)

The method based on the interpolation of the admittance is first presented. Following Shur et al. [26], we define a set of reference values for the rms velocity $v_{\text{rms}}^{(l)}$, $l = 1, 2, \dots, N$. This set covers the expected range of variation of v_{rms} and has to be adapted according to the problem under consideration. At each of these reference values $v_{\text{rms}}^{(l)}$, the frequency-dependent admittance $Y(\omega, v_{\text{rms}}^{(l)}) = [Z_{\text{NL}}(\omega, v_{\text{rms}}^{(l)})]^{-1}$ (see Eq. (3)) is approximated by a multipole model

$$Y^{(l)}(\omega) = Y(\omega, v_{\text{rms}}^{(l)}) = Y_{\infty}^{(l)} + \sum_{k=1}^{p^{(l)}} \frac{A_k^{(l)}}{\lambda_k^{(l)} - j\omega}, \quad (13)$$

where the same notation than in Eq. (10) is employed. The poles and coefficients of the admittances ($Y_{\infty}^{(l)}$, $A_k^{(l)}$ and $\lambda_k^{(l)}$) are determined for the reference values $v_{\text{rms}}^{(l)}$ using the VF algorithm. Note that the number of real poles and pairs of complex conjugate poles can vary depending on the rms velocity. Then, for any v_{rms} value in the range $[v_{\text{rms}}^{(1)}, v_{\text{rms}}^{(N)}]$, the admittance of the perforated panel ($Y(\omega, v_{\text{rms}})$) is calculated using a linear combination of the individual admittances at each of these reference values $v_{\text{rms}}^{(l)}$

$$Y(\omega, v_{\text{rms}}) = \sum_{l=1}^N \sigma_l(v_{\text{rms}}) Y^{(l)}(\omega) \quad \sum_{l=1}^N \sigma_l = 1, \quad (14)$$

where σ_l are the weights, that provide information about the rms velocity in the perforation.

As done by Shur et al. [26], the weights are obtained by linear interpolation between the defined reference values $v_{\text{rms}}^{(l)}$. Thus, for v_{rms} belonging into the range $v_{\text{rms}}^{(l-1)} \leq v_{\text{rms}} \leq v_{\text{rms}}^{(l)}$, the weights are calculated as follows:

$$\begin{cases} \sigma_l = \frac{v_{\text{rms}} - v_{\text{rms}}^{(l-1)}}{v_{\text{rms}}^{(l)} - v_{\text{rms}}^{(l-1)}} \\ \sigma_{l-1} = 1 - \sigma_l \\ \sigma_k = 0 \text{ for } k < (l-1) \text{ and } k > l \end{cases} \quad (15)$$

In the case where v_{rms} is outside the range of the reference values ($v_{\text{rms}} \leq v_{\text{rms}}^{(1)}$ or $v_{\text{rms}} \geq v_{\text{rms}}^{(N)}$), the admittance is set to the admittance at the corresponding end value of the velocity range, i.e. all the weights are equal to zero, except the weight of the end value which is equal to 1. Note that the linear interpolation is not a requirement of the method and that higher-order interpolation could be used.

It remains to evaluate v_{rms} from the numerical solution. To do so, the rms velocity is estimated at a given time t with the relation

$$\bar{v}_{\text{rms}}^2(t) = \frac{1}{t} \int_0^t v^2(t') dt', \quad (16)$$

where $v(t)$ is the velocity fluctuation in the orifice. Due to the conservation of the acoustic flow rate, it is equal to the ratio of the acoustic normal velocity on the liner to the POA, i.e. $v(t) = u_n(t)/\varphi$. Taking the time derivative of the above equation leads to the differential equation:

$$\frac{d(t\bar{v}_{\text{rms}}^2)}{dt} = \frac{u_n^2(t)}{\varphi^2}, \quad (17)$$

that is integrated in time with the time-marching scheme to obtain $\bar{v}_{\text{rms}}(t)$. In practice, a simpler approach is employed. The value of \bar{v}_{rms} at the time iteration n is calculated from its value at iteration $n-1$ using the recursive expression:

$$\bar{v}_{\text{rms}}^2(n\Delta t) = \left(1 - \frac{1}{n}\right) \bar{v}_{\text{rms}}^2[(n-1)\Delta t] + \frac{1}{n} \frac{u_n^2(n\Delta t)}{\varphi^2}, \quad (18)$$

with Δt the time step. This expression can be obtained by integrating Eq. (17) between two consecutive time steps and by assuming that u_n is constant over a time step.

Therefore, the nonlinear extension of the TDABC in Eq. (11) with the IA method is rewritten as follows

$$Z_0 u_n(t) = \sum_{l=1}^N \sigma_l(\bar{v}_{\text{rms}}) \left(Y_{\infty}^{(l)} p(t) + \sum_{k=1}^{p^{(l)}} A_k^{(l)} \phi_k^{(l)}(t) \right), \quad (19)$$

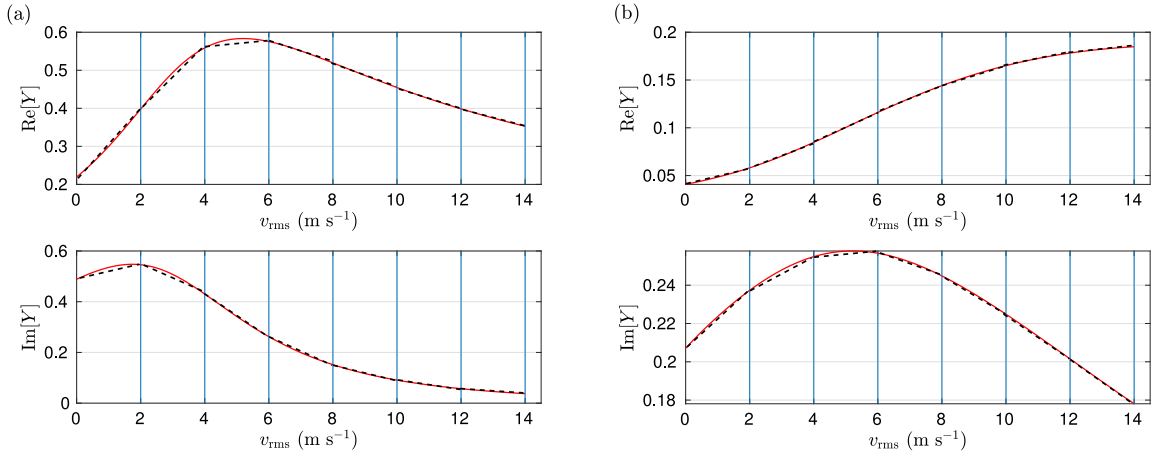


Fig. 3. Real and imaginary parts of the admittance for a frequency of (a) $f = 2000$ Hz and (b) $f = 3000$ Hz as a function of the rms velocity in the perforation for PP#1 absorber with a cavity depth of 10 mm calculated with Eq. (3) (solid line) and by linear interpolation (dotted line). The vertical lines at $v_{\text{rms}} = 0, 2, 4, 6, 8, 10, 12$ and 14 m s $^{-1}$ show the reference values used for the interpolation.

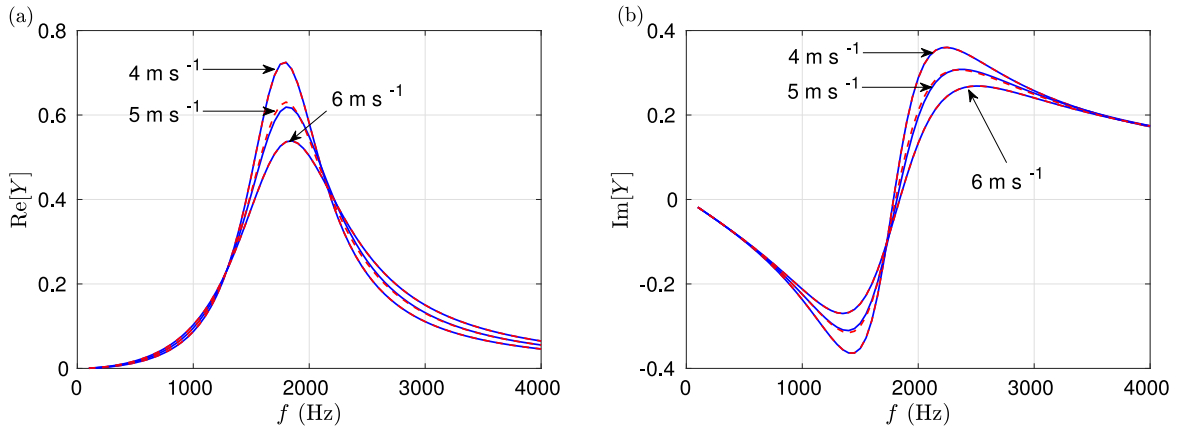


Fig. 4. (a) Real and (b) imaginary parts of the admittance of PP#1 absorber with a cavity depth of 10 mm as a function of the frequency for three rms velocities: exact calculation (solid blue line) and approximation with the IA method (dotted red line).

where the accumulators $\phi_k(t)$ are obtained by integrating the ODE:

$$\frac{d\phi_k^{(l)}}{dt} + \lambda_k^{(l)} \phi_k^{(l)}(t) = p(t) \quad (20)$$

and \bar{v}_{rms} by integrating Eq. (17).

In order to choose the set of reference values $v_{\text{rms}}^{(l)}$, the evolution of the admittance with the rms velocity in the perforation is investigated. Fig. 3 shows the normalized admittance (solid line) as a function of v_{rms} for PP#1 with a cavity depth of 10 mm and for two frequencies (2000 and 3000 Hz). It is seen that the nonlinear behavior is strongly dependent on the frequency: the variation with v_{rms} is significant for 2000 Hz, which is close to the resonant frequency of the PP liner, but limited for 3000 Hz. In addition, the admittance is not varying simply with v_{rms} . In order to use linear interpolation, it is necessary to choose a sufficiently small step between two consecutive reference values to represent correctly the variations of Y with v_{rms} . The dotted line thus corresponds to a linear interpolation using a step of 2 m s $^{-1}$. With this step, the interpolated admittance shows a good agreement with the exact admittance.

Fig. 4 shows the comparison between the exact admittance model and its approximation with the IA method for three rms velocities (4, 5, and 6 m s $^{-1}$). This velocity range is chosen because the error in Fig. 3 is maximum in this range. Note that $v_{\text{rms}} = 4$ and 6 m s $^{-1}$ are considered as reference values in the IA method: for these two rms velocities, the exact admittance is approximated by a multipole model using the VF algorithm. The approximation is performed for 200 Hz $< f < 4000$ Hz using two poles, which is seen to be sufficient to accurately represent the variation of Y over the entire frequency range of interest. For the intermediate rms velocity $v_{\text{rms}} = 5$ m s $^{-1}$, the admittance in the IA method is obtained by linear interpolation from the multipole models at $v_{\text{rms}} = 4$ and 6 m s $^{-1}$. Here also, a close agreement with the exact admittance is observed.

Table 2

Number of real poles and pairs of complex conjugate poles for the reference values $v_{rms}^{(l)}$ and for the three PPs absorbers.

PP#1, PP#3													
Cavity depth (mm)		10						30					
Reference rms velocity (m s ⁻¹)		2	4	6	8	10	12	2	4	6	8	10	12
Incident SPL (dB)		114	122	128	132	135	138	114	122	128	132	135	138
Poles number	Real	0	0	0	0	0	0	0	0	0	0	0	0
	Complex conjugate pair	1	1	1	1	1	1	1	1	1	1	1	1
PP#2													
Cavity depth (mm)		10						30					
Reference rms velocity (m s ⁻¹)		2	4	6	8	10	12	2	4	6	8	10	12
Incident SPL (dB)		112	121	127	131	134.5	137.5	112	121	127	131	134.5	137.5
Poles number	Real	0	0	0	0	0	0	0	0	0	0	2	2
	Complex conjugate pair	1	1	1	1	1	1	1	1	1	1	0	0

In accordance with the discussion around Fig. 3, we have chosen the set of reference values for the rms velocity $v_{rms}^{(l)} = 2, 4, 6, 8, 10$ and 12 m s^{-1} with $N = 6$. For each reference value, the admittance is fitted over the frequency range 200–4000 Hz by a multipole model using the VF algorithm with two poles. The number of real poles and of pairs of complex conjugate poles for the reference values is indicated in Table 2 for the three PPs absorber. The related incident sound pressure levels (SPL) is also indicated. It represents the SPL of the incident wave, that generates the corresponding rms velocity in the perforation. It is estimated from the relation derived by Ingard [36] that expresses the rms incident pressure $p_{i,rms}$ as a function of v_{rms} :

$$p_{i,rms} = \frac{\rho_0 c_0^2}{2} \frac{\varphi v_{rms}}{c_0} \left(1 + \frac{1 - \varphi^2}{\varphi} \frac{\sqrt{2} v_{rms}}{c_0} \right) \tag{21}$$

This expression is valid only at the resonant frequency of the PP, for which the velocity in the perforation is maximum for a given incident SPL. To reach the same value of v_{rms} at frequencies different from the resonant frequency, a larger incident SPL is necessary. Therefore, the SPL indicated in Table 2 has to be interpreted as the minimum incident SPL generating the corresponding value of the velocity in the perforation. For information, the poles and coefficients of the multipole model used for the IA method are indicated in Table A.4 in Appendix A for PP#1 with the cavity depths of 10 and 30 mm.

The main disadvantage of this method can be brought to light. For v_{rms} outside the range of the reference values, it is not possible to evaluate correctly the admittance. The range covered by the reference values has thus to be broadened considerably to avoid such cases. In addition, to represent accurately the variation of the admittance with v_{rms} , the step between two successive reference values should be sufficiently small. Therefore, the number of reference values and, hence, of poles can be significant with the IA method, which can lead to an increase in the computational cost. For PP liners, the admittance can be approximated over a broad range of frequencies using few poles: the cost of the IA method is thus moderate. For other types of liner, this can become a shortcoming of the IA method.

3.4.2. Interpolation of the admittance parameters (IAP)

In this section, a new approach to account for the nonlinear effects on the admittance is proposed. To do so, the admittance is still written as a multipole model, as in Eq. (10), but the coefficients and the poles are allowed to vary with v_{rms} . This gives:

$$Y(\omega, v_{rms}) = Y_\infty(v_{rms}) + \sum_{k=1}^P \frac{A_k(v_{rms})}{\lambda_k(v_{rms}) - j\omega} \tag{22}$$

It is then necessary to calculate the poles and coefficients of the multipole model as a function of v_{rms} . To do so, one idea could be to couple the VF algorithm and the time-domain numerical model, so that the poles and the coefficients of the admittance are determined dynamically as the value of \tilde{v}_{rms} changes. This would however require to run the VF algorithm after each iteration (or after each step of the Runge–Kutta algorithm). Even if the VF algorithm usually takes few tenths of a second to run, this would add complexity and computational cost to the approach. Especially for multi-dimensional problems, it would be necessary to run the VF algorithm for each grid point on the liner. A more efficient strategy is to have an approximate analytical expression giving the evolution of the poles and coefficients of Y with v_{rms} . In this work, the multipole coefficients (real and imaginary parts, separately) are approximated by a rational function with quadratic polynomials. For example, one has:

$$Y_\infty(v_{rms}) = \frac{Y_\infty^{n,0} + Y_\infty^{n,1} v_{rms} + Y_\infty^{n,2} v_{rms}^2}{1 + Y_\infty^{d,1} v_{rms} + Y_\infty^{d,2} v_{rms}^2} \tag{23}$$

where $Y_\infty^{n,0}, Y_\infty^{n,1}, Y_\infty^{n,2}, Y_\infty^{d,1}$ and $Y_\infty^{d,2}$ are constants. A similar expression holds for $\text{Re}[A_k(v_{rms})], \text{Im}[A_k(v_{rms})], \text{Re}[\lambda_k(v_{rms})]$, and $\text{Im}[\lambda_k(v_{rms})]$. The rational function approximation is determined using the curve fitting toolbox of MATLAB (with data points obtained with the VF algorithm for $0 \leq v_{rms} \leq 12 \text{ m s}^{-1}$ with a step of 1 m s^{-1}). Other approaches, such as the VF algorithm, could also have been employed. As an example, the poles and coefficients of the multipole function are plotted as a function of v_{rms}

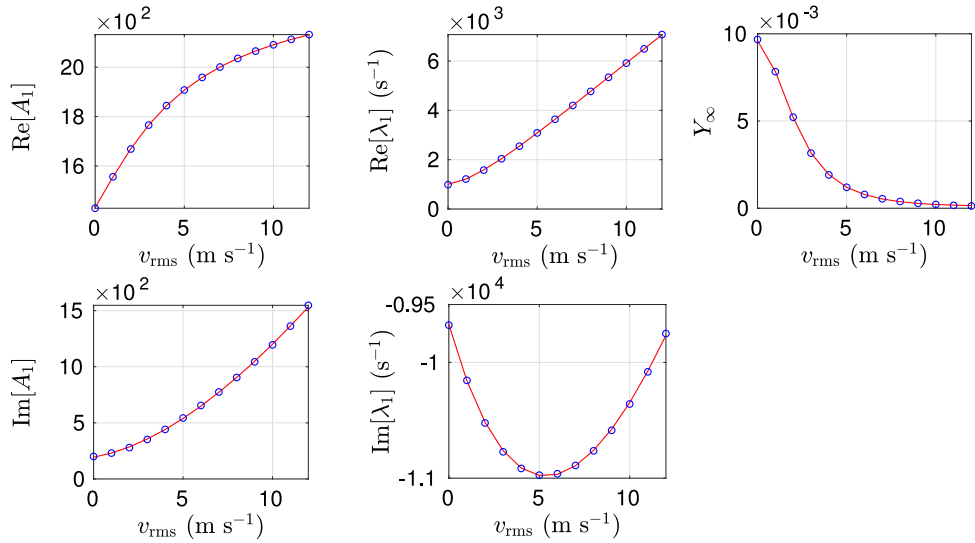


Fig. 5. Coefficients of the multipole model as a function of the rms velocity v_{rms} (blue circle symbols) and their approximation (red solid lines) using a rational function (PP#1 for a cavity depth of 10 mm).

in Fig. 5 along with their rational function approximation for PP#1 with a cavity depth of 10 mm. The constants of the rational function approximation for the multipole coefficients are given in Appendix A in Table A.5 for PP#1 liner with the two cavity depths of 10 and 30 mm.

With the expression of the admittance in Eq. (22), the nonlinear extension of the TDABC in Eq. (11) with the IAP method is defined as follows:

$$Z_0 u_n(t) = Y_\infty(\bar{v}_{rms})p(t) + \sum_{k=1}^P A_k(\bar{v}_{rms})\phi_k(t), \quad (24)$$

where the function ϕ_k is governed by the ODE:

$$\frac{d\phi_k}{dt} + \lambda_k(\bar{v}_{rms})\phi_k(t) = p(t) \quad (25)$$

and \bar{v}_{rms} is determined from Eq. (17).

The IAP method is simpler to implement than the IA method. One difficulty is that, while in the VF algorithm, the total number of poles can be chosen, it is not possible to set their type (real poles or pair of complex conjugate poles). Therefore, a pair of complex conjugate poles can switch to two real poles for a given value of v_{rms} and inversely. Thus, the number of each type of poles is constant in all cases considered for rms velocities in the perforations between 0 and 12 m s⁻¹, except for PP#2 with a cavity depth of 30 mm for which it changes from 10 m s⁻¹ (see Table 2). As a consequence, the variation of the poles and coefficients A_k and λ_k with v_{rms} is discontinuous when the poles type changes. A simple method to handle this issue with the IAP method is to define the poles and coefficients A_k and λ_k as piecewise rational functions of v_{rms} with a different set of coefficients for velocities for which the poles are real and for velocities for which the poles come as complex conjugate pairs. This approach has been tested for the impedance tube configuration, detailed in Section 4. It was shown to be effective but induced a longer transient before convergence. Results are not shown for conciseness. Because this issue was only noticed for PP#2 with a cavity depth of 30 mm and for a large velocity in the perforations, further investigation is left for future work.

4. 1D validation

The present section aims to verify that the proposed methods in Section 3.4 allow for an accurate representation of the surface impedance in the nonlinear regime. For that, the one-dimensional configuration corresponding to an impedance tube is considered, as shown in Fig. 2. Numerical experiments are first presented in Section 4.2 and comparisons to measurements are then performed in Section 4.3. The MATLAB codes employed for the numerical experiments with the IAP method are available in the supplementary material.

4.1. Numerical parameters

The computational domain ($0 \leq x \leq L$) is discretized by 101 points with a uniform spatial step $\Delta x = 0.0085$ m. The total simulation time is $t_{max} = 0.3$ s. The CFL (Courant–Fridrichs–Lewy) number is set to 0.5, which gives a time step $\Delta t = 1.25 \times 10^{-5}$ s.

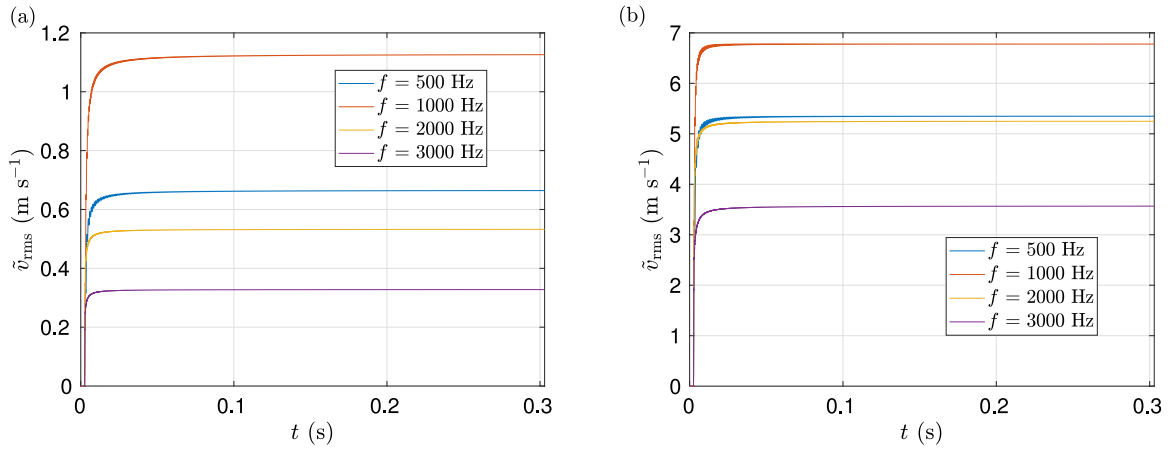


Fig. 6. Time-variation of the estimated rms velocity in the perforation \bar{v}_{rms} for PP#1 absorber with a cavity depth of 30 mm and for two incident SPL: (a) $SPL_i = 110$ dB and (b) $SPL_i = 130$ dB.

Numerical simulations are carried out for two types of incident waves, namely a harmonic and a broadband wave. For the former case, the incident wave is $p_i(t) = \sqrt{2} p_{i,rms} \sin(2\pi f t)$, where $p_{i,rms}$ is the rms value. For the latter case, the incident wave is $p_i(t) = p_{i,rms} s(t)$, where $s(t)$ is a broadband stationary signal of unitary rms value. The incident SPL is also used thereafter to characterize the excitation and is defined by:

$$SPL_i = 20 \log_{10} \left(\frac{p_{i,rms}}{p_{ref}} \right) \quad (26)$$

with the reference pressure set to $p_{ref} = 2 \times 10^{-5}$ Pa.

The two-microphone method is employed to estimate the surface impedance of the PP liner (Z) for both the numerical simulations and the experiments. The normalized surface impedance is determined from the frequency response function H_{12} between two microphones at positions x_1 and x_2

$$Z = -j \frac{\sin[k_0(l-s)] - H_{12} \sin(k_0 l)}{H_{12} \cos(k_0 l) - \cos[k_0(l-s)]}, \quad (27)$$

where $l = L - x_1$ and $s = |x_1 - x_2|$. For the numerical simulations, the frequency response function H_{12} is obtained directly by the ratio of the Fourier transforms of the time pressure signals at positions x_1 and x_2 , in the case of harmonic excitation and by the ratio of the cross power spectral density of the time pressure signals at positions x_1 and x_2 to the power spectral density at x_2 , in the case of broadband excitation.

4.2. Numerical experiment

4.2.1. Harmonic excitation

The case of a harmonic excitation is first treated. Simulations are performed for incident waves with the same SPL and with frequencies between 200 and 4000 Hz, in steps of 100 Hz. At the initial time $t = 0$, all variables are set to zero, including \bar{v}_{rms} . Once the incident wave impinges on the liner, \bar{v}_{rms} increases. This modifies the surface impedance which in turn induces a variation of the acoustic field and of \bar{v}_{rms} . This process repeats itself until a steady-state is obtained. This can be checked by looking at the convergence of \bar{v}_{rms} , i.e. when the difference between the values of \bar{v}_{rms} at two successive iterations becomes sufficiently small ($\approx 10^{-3}$ m s $^{-1}$). Fig. 6 shows the time-variation of the estimated rms velocity for four frequencies (500, 1000, 2000, 3000 Hz) at two incident SPL (110 and 130 dB) using PP#1. It is seen that \bar{v}_{rms} monotonously increases with time and that convergence is reached from $t = 0.2$ s for all cases. In addition, it can be noted that the rms velocity strongly depends on the frequency.

Fig. 7 shows the rms velocity as a function of the frequency for PP#1 absorber for two cavity depths and for several incident SPL. The maximum of velocity is obtained near the resonant frequency and the latter is slightly shifted towards the high frequencies with the increase of the incident SPL. The variations of the rms velocity with the frequency for the two other absorbers PP#2 and PP#3 are similar but they are not shown for conciseness.

The real and imaginary parts of the admittance estimated from the numerical simulation with the IA and IAP methods are shown in Figs. 8 and 9 for PP#1 and PP#3 with two cavity depths and for several incident SPL. It is seen that the surface admittance is significantly different depending on the incident SPL: in particular, increasing the incident SPL tends to flatten the curves. The corresponding analytical admittances calculated from Eq. (3) are also plotted in Figs. 8 and 9. Note that the rms velocity in the perforations determined from the numerical solution is used as input data for the analytical admittance model. For both IA and IAP methods, the numerical results are in good agreement with the analytical results over the entire frequency range for the reference values as well as for the intermediate values of the velocity. This shows that both methods allow for an accurate representation of the nonlinear admittance in the time domain.

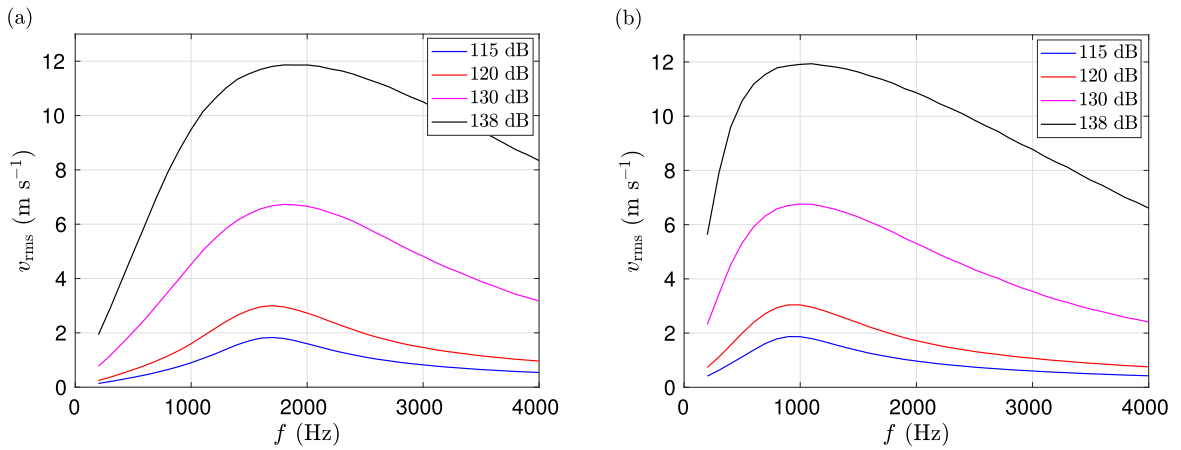


Fig. 7. Variation of the rms velocity in the perforation with the frequency for several incident SPL and for PP#1 with two cavity depths: (a) $D = 10$ mm and (b) $D = 30$ mm.

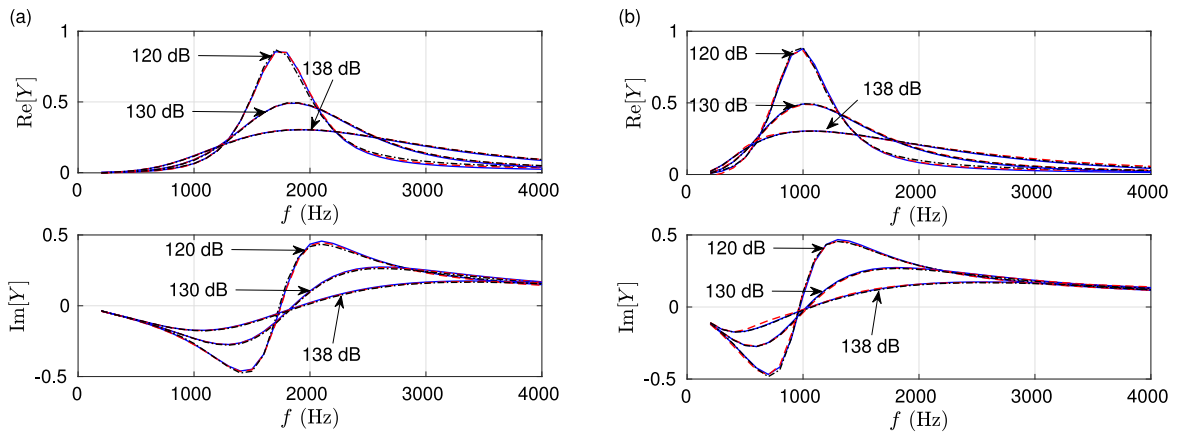


Fig. 8. Admittance for PP#1 absorber with a cavity depth of (a) $D = 10$ mm and (b) $D = 30$ mm: calculated with the analytical model in Eq. (3) (blue solid) and determined from the numerical solution using the IAP (red dashed) and the IA (black dash-dotted) methods. A harmonic excitation is used.

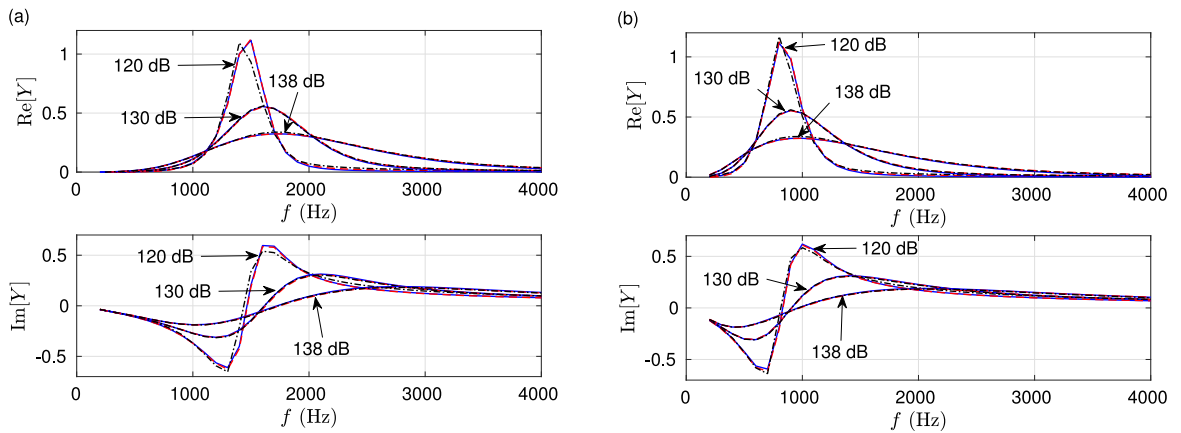


Fig. 9. Admittance for PP#3 absorber with a cavity depth of (a) $D = 10$ mm and (b) $D = 30$ mm: calculated with the analytical model in Eq. (3) (blue solid) and determined from the numerical solution using the IAP (red dashed) and the IA (black dash-dotted) methods. A harmonic excitation is used.

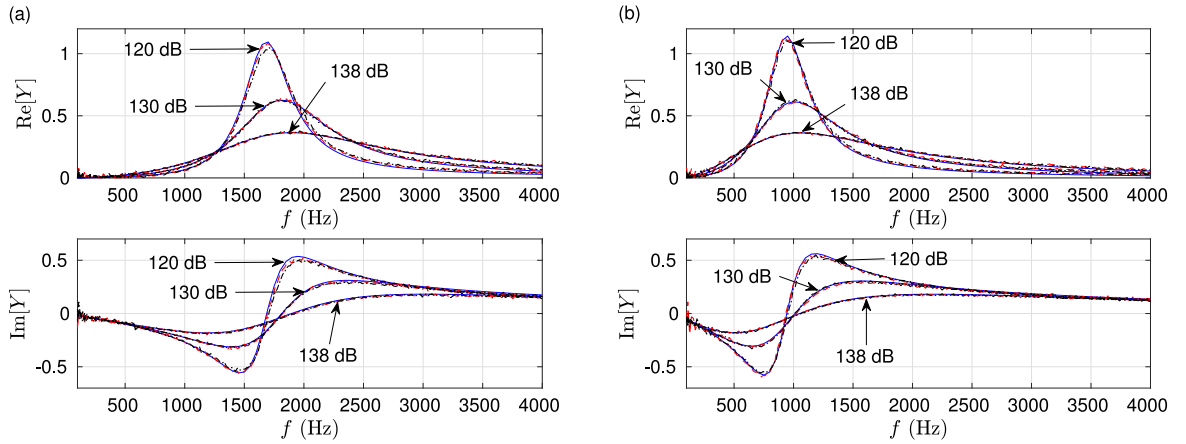


Fig. 10. Admittance for PP#1 absorber with a cavity depth of (a) $D = 10$ mm and (b) $D = 30$ mm: calculated with the analytical model in Eq. (3) (blue solid) and determined from the numerical solution using the IAP (red dashed) and the IA (black dash-dotted) methods. A broadband excitation is used.

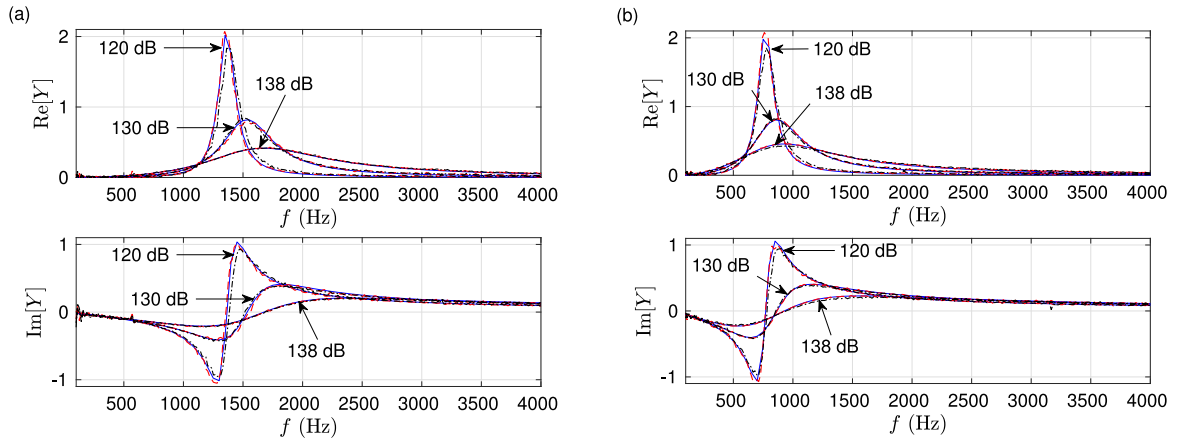


Fig. 11. Admittance for PP#3 absorber with a cavity depth of (a) $D = 10$ mm and (b) $D = 30$ mm: calculated with the analytical model in Eq. (3) (blue solid) and determined from the numerical solution using the IAP (red dashed) and the IA (black dash-dotted) methods. A broadband excitation is used.

4.2.2. Broadband excitation

In this section, the case of a broadband excitation is studied. A white noise filtered using a Butterworth bandpass filter with lower and upper cutoff frequencies of 200 Hz and 4000 Hz, respectively, is employed.

The admittance determined from the numerical solution using the two methods IA and IAP is shown in Figs. 10 and 11 for PP#1 and #3 with two cavity depths and for three incident SPL. The dependence of the surface admittance in the nonlinear regime with the characteristics of the incident signal can be first noticed by comparing these two figures with Figs. 8 and 9. Indeed, the surface admittance for the harmonic excitation is significantly different from that for the broadband excitation, despite that the incident SPL on the liner is the same. In particular, for PP#3 (Figs. 9 and 11), the admittance amplitude for the broadband excitation is almost two times larger than for the harmonic excitation.

Second, the analytical admittance in Eq. (3) is also plotted in Figs. 10 and 11. Here as well, the rms velocity in the perforations deduced from the numerical simulation is used for the calculation of the analytical admittance. As a reminder, v_{rms} is a single value for the broadband admittance spectrum. As an example, for PP#1 absorber with a cavity depth of 10 mm, v_{rms} is equal to 1.8, 5 and 9.6 $m s^{-1}$ for incident SPL of 120, 130 and 138 dB, respectively. For the three incident sound pressure levels of 120, 130 and 138 dB, the predicted real and imaginary parts of the admittance are in good agreement with the analytical results for both PPs absorber with two cavity depths of 10 and 30 mm. The comparison is more favorable to the IAP method than to the IA method, which may be due to the low-order interpolation used in the IA method.

4.3. Experimental validation

As a last check, numerical results with the nonlinear TDABC are compared to experimental results.

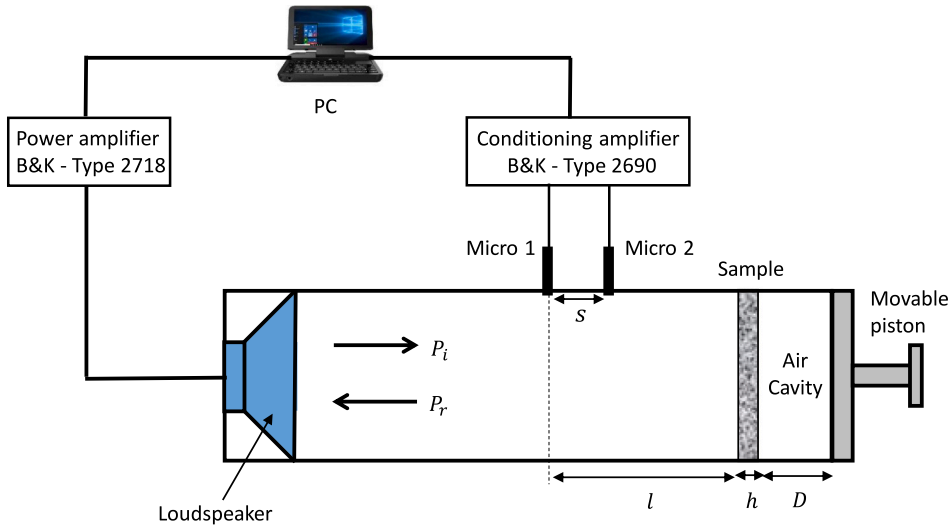


Fig. 12. Schematic diagram of the impedance tube for measuring the surface admittance of a sample by using the two-microphone transfer-function method.

The measurements were performed using a B&K Type 4206 impedance tube kit, as illustrated in Fig. 12. The tube has a circular cross-section, with an inner diameter of 3 cm, yielding a cut-off frequency around 6400 Hz. The sample plate is located at the right hand side of the tube. An air cavity of depth D is created behind the plate by a movable piston which is used as a rigid backing wall. Two sets of measurements were made, considering a harmonic excitation and a broadband excitation. For harmonic excitation, acoustic waves were generated by a loudspeaker mounted at the left hand side of the tube. For broadband excitation, the loudspeaker of the impedance tube kit was replaced by a JBL 2447H compression driver. The acoustic sources were powered by a B&K power amplifier type 2718. Pressure signals were measured using two flush-mounted $1/4''$ microphones (B&K type 4187), associated to two B&K type 2670 preamplifiers, a conditioning amplifier type 2690, and National Instrument 9250 front-end. An amplitude and phase calibration method was used to correct the transfer function between the two measurement channels.

The two-microphone method [37], as described in Section 4.1, was used to determine the surface impedance of the PP sample. The distance between the sample and the microphone 1 is $l = 55$ mm and the two microphones were separated by a distance $s = 20$ mm.

4.3.1. Harmonic excitation

The measurements were carried out for the three PP absorbers described in Section 2 using a harmonic excitation over a frequency range between 500 and 4000 Hz in steps of 50 Hz. Two levels of excitation, corresponding to two different gains of the power amplifier, were considered. In the first case, denoted as the low SPL case, the amplifier gain was set to ensure that the SPL inside the tube was sufficiently small to be in the linear regime, while maintaining a good signal-to-noise ratio for all frequencies. In the second case, denoted as the high SPL case, the amplifier gain was increased to its maximum, while ensuring negligible harmonic distortion.

In the literature, measurements to characterize perforated plates at high SPL are rather performed by keeping the same level of the incident wave on the plate (see, e.g., Refs. [12,38]), as done in the numerical experiments in Section 4.2.1. As we are mostly interested in validating the numerical model proposed in Section 3, this was not deemed necessary in this study.

A quantitative information on the acoustic excitation of the PP plate can be determined from the measurements. To do so, the acoustic pressure and velocity in the tube are expressed under the plane wave hypothesis as

$$P(x, \omega) = P_i(\omega)e^{jk_0x} + P_r(\omega)e^{-jk_0x} \quad U(x, \omega) = \frac{1}{Z_0} [P_i(\omega)e^{jk_0x} - P_r(\omega)e^{-jk_0x}] \quad (28)$$

where P_i and P_r represent the amplitude of the incident and reflected pressure waves in the tube, respectively. They can be determined thanks to the two-microphone method, with the relations:

$$P_i = jP(x_1) \frac{e^{-jk_0x_2} - H_{12} e^{-jk_0x_1}}{2 \sin(k_0s)} \quad P_r = -jP(x_1) \frac{e^{jk_0x_2} - H_{12} e^{jk_0x_1}}{2 \sin(k_0s)}. \quad (29)$$

Fig. 13 shows the amplitude of the incident wave $|P_i|$ for PP#1 absorber with a cavity depth of 30 mm as a function of the driving frequency for the low and the high SPL cases. Although it can be expected that the amplitude of the acoustic wave generated by the loudspeaker is constant over the entire frequency range, the amplitude of the incident wave greatly varies with the frequency. The incident pressure is maximal for some frequencies; this could be related to the resonant frequencies of the tube. For the low SPL case, $|P_i|$ is below 9 Pa for all frequencies corresponding to incident SPL below 110 dB. For the high SPL case, $|P_i|$ reaches a maximum of 122 Pa for $f = 2850$ Hz, corresponding to an incident SPL of about 133 dB.

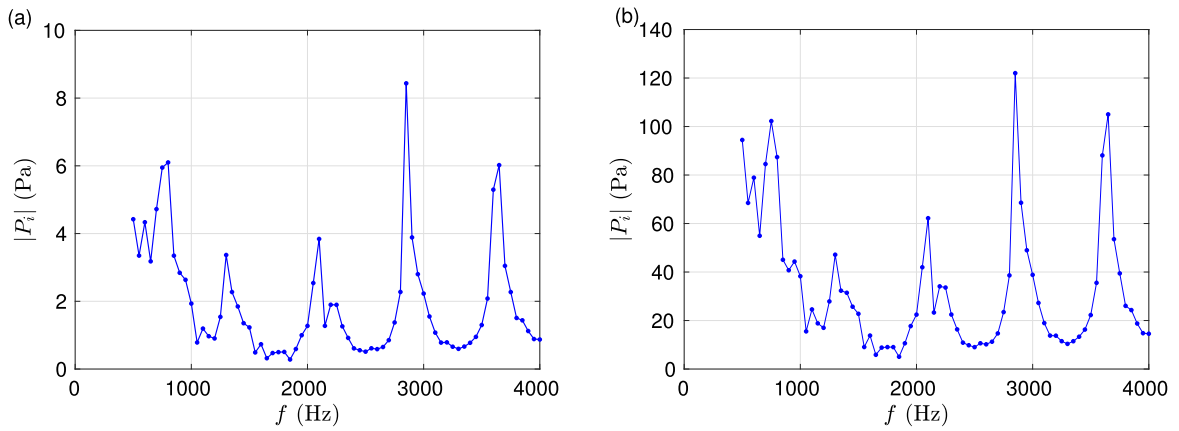


Fig. 13. Measured amplitude of the incident acoustic pressure for PP#1 absorber with a cavity depth of 30 mm for (a) low and (b) high SPL cases.

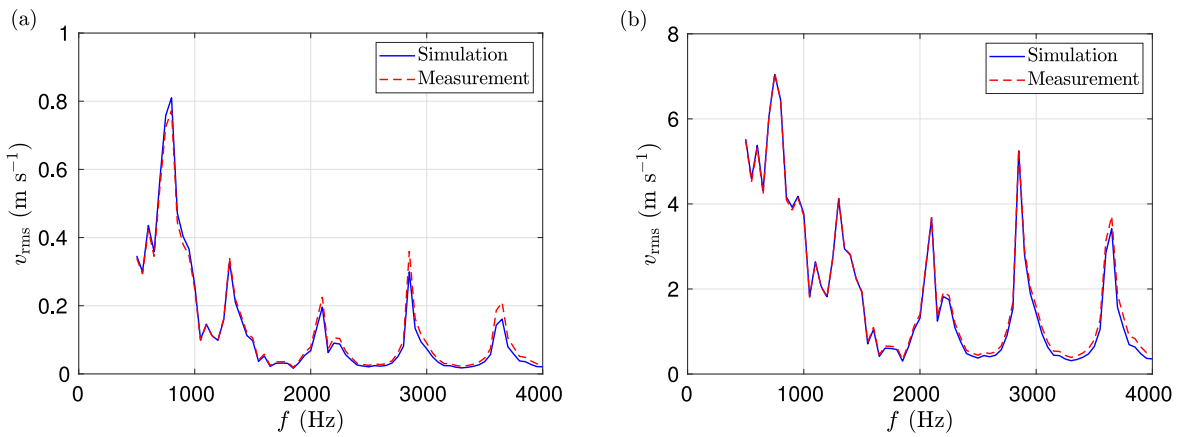


Fig. 14. Rms amplitude of the velocity in the perforations for a harmonic excitation determined from the experiments and from the numerical simulation for PP#1 absorber with a cavity depth of 30 mm for the (a) low and (b) high SPL cases.

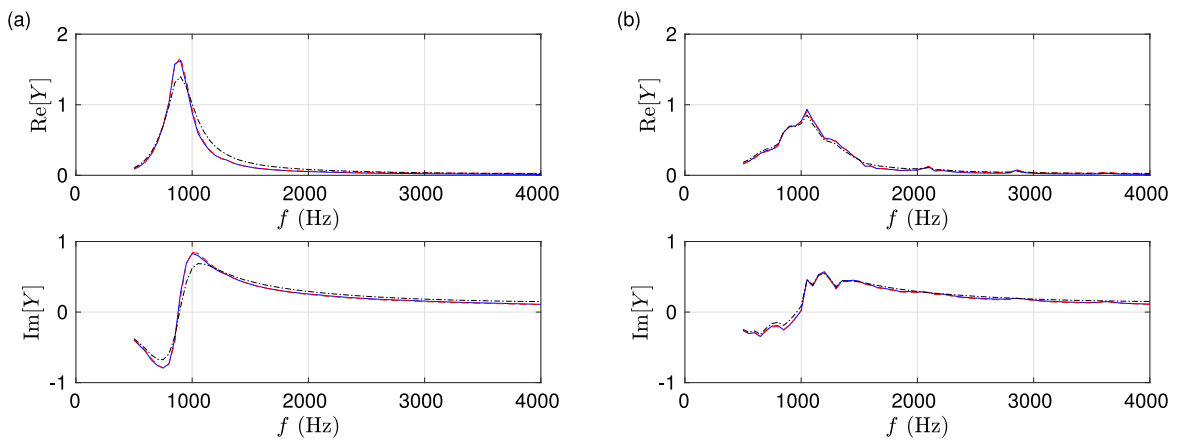


Fig. 15. Surface admittance of PP#1 absorber with a cavity depth of 30 mm for a harmonic excitation for the (a) low and (b) high SPL cases: measured (black dash-dotted) and determined from the analytical model in Eq. (3) (blue solid) and from the numerical solution (red dashed).

The numerical simulations are performed using the IAP method for the TDABC. In addition to the nonlinear surface admittance model of the PP liner, the amplitude of the incident wave has to be prescribed. It is set to the value determined in the experiments, i.e. $p_{i,rms} = |P_i|/\sqrt{2}$.

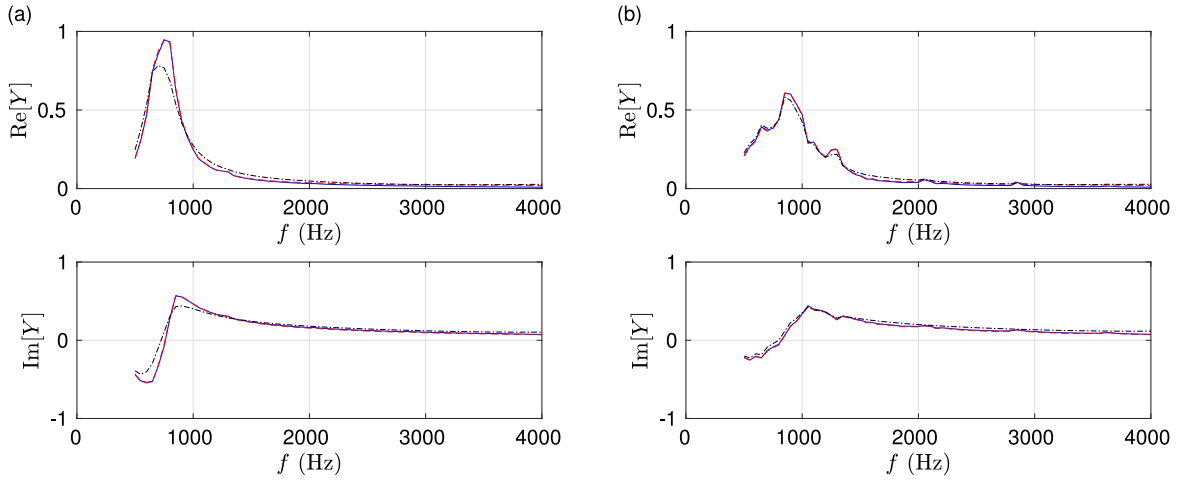


Fig. 16. Surface admittance of PP#2 absorber with a cavity depth of 30 mm for a harmonic excitation for the (a) low and (b) high SPL cases: measured (black dash-dotted) and determined from the analytical model in Eq. (3) (blue solid) and from the numerical solution (red dashed).

The comparison between the experimental and numerical results is now presented. The rms amplitude of the velocity in the perforations is shown in Fig. 14 both for the experiments and for the numerical solution and for PP#1 with a cavity depth of 30 mm. Note that the experimental value of v_{rms} is determined from the pressure measurements with the two microphones using Eq. (28), which yields $v_{rms} = |U(x=L)|/(\sqrt{2}\rho)$. An excellent agreement is seen at both low and high SPL. In addition, the frequency of the peaks observed in Fig. 14 is in accordance with those of the incident pressure amplitude in Fig. 13.

The experimental admittances obtained for PP#1 and #2 are shown in Figs. 15 and 16, respectively, along with those determined from the numerical models for the two levels of excitation. Both are determined with the two-microphone method using Eq. (27). The analytical admittance obtained with the Laly model using the rms velocity in the perforations determined from the measurements is also plotted. A good agreement is obtained between the measurements and the numerical and analytical models, especially for the high SPL case. We can also note the difference in the real and imaginary parts of the admittance between the low and the high SPL cases, due to the nonlinear effect. In addition, the abrupt variations of the surface admittance observed for the high SPL case are due to the corresponding variations of the incident pressure with the frequency.

4.3.2. Broadband excitation

The measurements were repeated for the three PPs absorbers using a white noise signal as the excitation signal and for several levels of excitation. Results are exemplified below for PP#1 absorber with a cavity depth of 30 mm. The comparisons for PP#2 and PP#3 both with a cavity depth of 30 mm are shown in Appendix B.

Information on the incident pressure has to be obtained from the experiments for the numerical simulations. With this aim, the power spectral density of the incident pressure S_{ii} is calculated from those of the pressure at the two microphones based on Eq. (29). For comparison purpose, the power spectral density of the velocity in the perforations S_{vv} is also calculated on the basis of Eq. (28). Only the part of the spectra below the tube cutoff frequency, i.e. for $f < 6400$ Hz, is considered. The power spectral densities are shown in Fig. 17. The spectrum of the incident pressure is not flat in the experiments, probably due to the resonances of the impedance tube, as already noticed for the harmonic excitation in Section 4.3.1. This is also the case for the spectrum of the velocity in the perforations. Note that the variations of S_{vv} with the frequency is slightly different from that of S_{ii} . The rms values of the incident pressure and velocity in the perforations are then estimated by integrating the corresponding power spectral density from 100 Hz up to 6400 Hz.

The numerical simulations are carried out using the IAP method for the TDABC. The incident pressure signal is a random signal, built so that its power spectral density is equal to the one measured. It induces in particular that the rms value of the incident pressure is the same in the simulations and in the experiments.

Fig. 18 shows the surface admittance determined from the measurements for three incident SPL: 76.4 dB in (a), corresponding to the linear regime, and 126.4 dB and 133.1 dB in (b) and (c), respectively, corresponding to the nonlinear regime. The variations of the surface admittance with the incident SPL are similar to those observed in Section 4.2.2: the amplitude of the real and imaginary parts of Y decreases and the peak of $\text{Re}[Y]$ widens with the increase of the incident SPL. The surface admittance deduced from the numerical simulations is also plotted in Fig. 18. While the match is not perfect with the measurements, a close agreement is noted. In particular, the evolution of the admittance with the incident SPL is well reproduced. Finally, the analytical model in Eq. (3) is also represented using the rms velocity in the perforations determined from the numerical simulations as input.

As an additional comparison, the corresponding absorption coefficients α are plotted in Fig. 19 for the three incident SPL. The impact of the incident SPL on the measured absorption coefficient is noticeable: the absorption bandwidth broadens and the maximum of α reduces with the increase of the incident SPL. Some ripples are seen in Figs. 19(b) and (c) near 1800 Hz in the

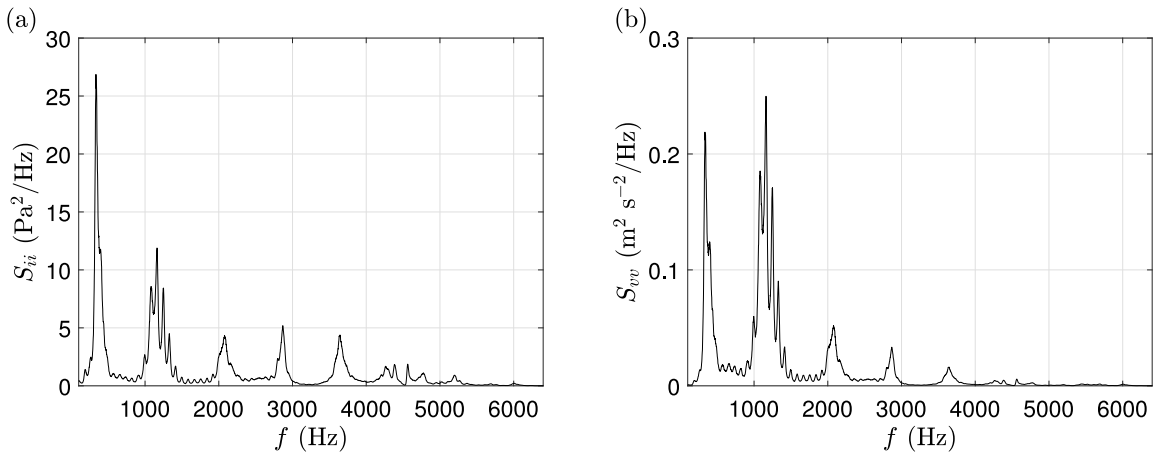


Fig. 17. One-sided power spectral densities of (a) the incident pressure and (b) the velocity in the perforations for PP#1 absorber with a cavity depth of 30 mm. A broadband excitation is used.

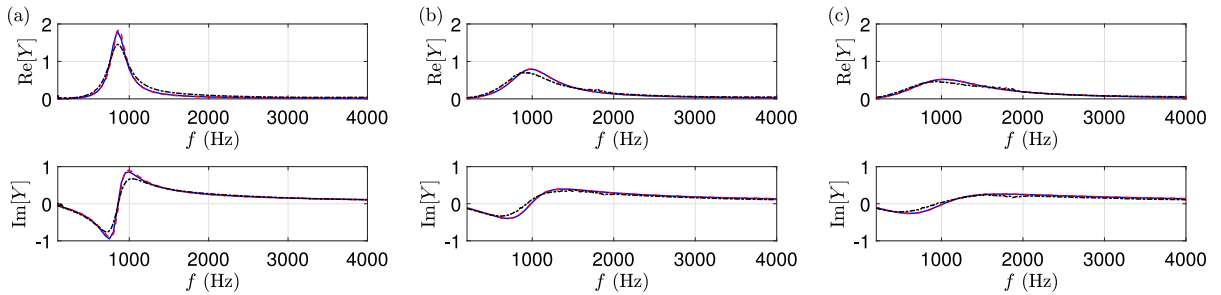


Fig. 18. Surface admittance of PP#1 absorber with a cavity depth of 30 mm for a broadband excitation and for three incident SPL (a) 76.4 dB, (b) 126.4 dB and (c) 133.1 dB: measured (black dash-dotted) and determined from the analytical model in Eq. (3) (blue solid) and from the numerical solution (red dashed).

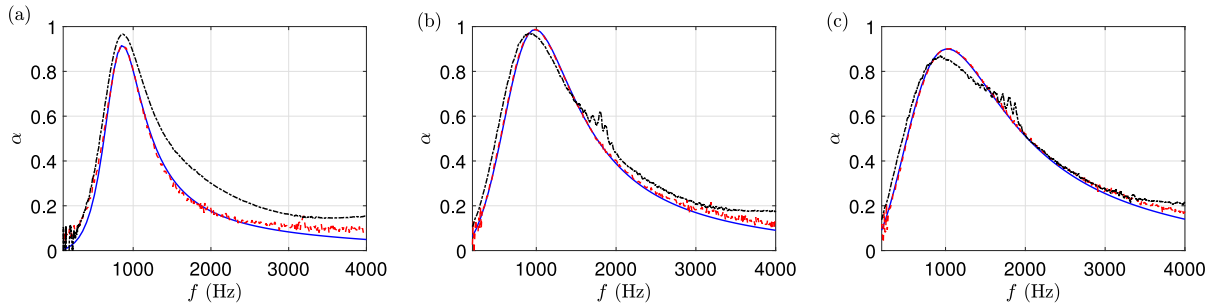


Fig. 19. Absorption coefficient of PP#1 absorber with a cavity depth of 30 mm for a broadband excitation and for three incident SPL (a) 76.4 dB, (b) 126.4 dB and (c) 133.1 dB: measured (black dash-dotted) and determined from the analytical model in Eq. (3) (blue solid) and from the numerical solution (red dashed).

Table 3

Rms amplitude of the velocity in the perforations for PP#1 absorber with a cavity depth of 30 mm for a broadband excitation: values deduced from the experiments and from the numerical simulations.

Incident SPL (dB)		76.4	86.2	96.7	106.0	116.2	126.4	133.1
v_{rms} (m s ⁻¹)	exp.	1.24×10^{-2}	3.69×10^{-2}	1.21×10^{-1}	3.56×10^{-1}	1.14	3.37	6.44
	num.	1.49×10^{-2}	4.86×10^{-2}	1.60×10^{-1}	4.54×10^{-1}	1.35	3.56	6.36

experimental curves; they are related to a lack of coherence due to low values of pressure at the microphones in this frequency range. The absorption coefficient determined from the numerical and analytical models are in good agreement with the measured one. While the curves of α are not superimposed, the numerical simulations capture especially the evolution of the absorption coefficient with the increase of the incident SPL.

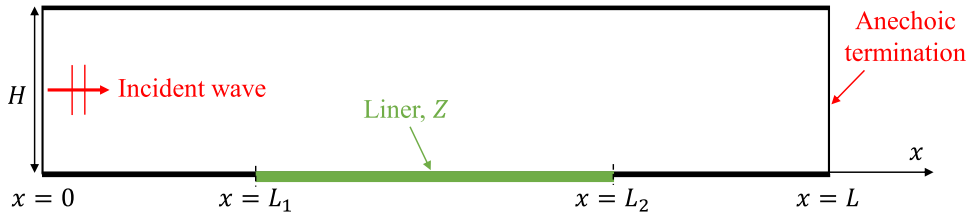


Fig. 20. Schematic of the 2D lined duct.

Finally, the rms amplitude of the velocity in the perforations deduced from the experiments and from the numerical simulations is reported in Table 3 for several incident SPL. It is observed that v_{rms} is noticeably well predicted from the numerical simulations.

5. Application to a 2D lined duct

This section is concerned with a two-dimensional (2D) lined duct, which is representative of industrial applications. The objectives are to evaluate the numerical model including the nonlinear TDABC in this situation as well as to analyze the impact of nonlinear TDABC on sound propagation and attenuation in a 2D lined duct. In particular, the nonlinear admittance model of PP liners depends on the velocity in the perforations. It is expected that this quantity varies significantly along the treatment and, as a consequence, that it is also the case for the surface admittance. Most of the existing methods for predicting sound propagation in a duct however consider a treatment with a uniform admittance. It is therefore worthwhile to investigate whether accounting for the spatial variations of the admittance at high excitation level is important for predicting the transmission loss in a lined duct.

5.1. Numerical configuration

A 2D lined duct of size $L \times H = 0.812 \text{ m} \times 0.0508 \text{ m}$ is considered, as shown in Fig. 20. The liner of length 0.406 m is located on the duct lower wall from $x = L_1 = 0.203 \text{ m}$ to $x = L_2 = 0.609 \text{ m}$. The other duct walls are rigid. This geometry corresponds to that of the Grazing Incidence Tube of NASA (see, e.g., Ref. [39]), which is one of the well-known duct facility for evaluating liner efficiency. There is no flow and the sound speed and air density are constant.

All the results presented in this section are obtained for the PP#1 absorber with a cavity depth of 10 mm. The frequency range of interest is between 200 Hz and 3000 Hz, which respects the cut-off frequency (around 3.35 kHz) of the duct. Two types of incident pressure waveforms, i.e. harmonic and broadband, are considered. The broadband signal is obtained by filtering a white noise signal using a Butterworth bandpass filter with lower and upper cutoff frequencies set to 200 Hz and 3000 Hz, respectively.

The 2D LEEs are solved using the numerical methods presented for the 1D case in Section 3.2. At the boundary $x = 0$, an incident plane wave propagating along the x -direction is generated using the method of characteristics, as described in Section 3.2. At $x = L$, a non-reflecting boundary condition is applied, using also the method of characteristics: the idea is the same, except that the incoming characteristic variable into the computational domain at the interface is set to zero so that no reflected waves are generated at the boundary. Finally, the normal velocity is set to zero on the duct rigid walls and the TDABC is applied along the lined section using the interpolation of the admittance parameters (IAP) approach presented in Section 3.4.2.

The mesh is uniform in the x -direction with a size $\Delta x = 1.1 \times 10^{-3} \text{ m}$. Along the z -direction, the mesh size is progressively reduced towards the liner walls with a stretching factor of 0.99. It is equal to $\Delta z = 1.1 \times 10^{-3} \text{ m}$ at the duct axis and $\Delta z = 8.19 \times 10^{-4} \text{ m}$ on the walls. The time step is set to $\Delta t = 2 \times 10^{-6} \text{ s}$, which yields a CFL number of 0.84. The total simulation time is 0.02 s for the harmonic excitation. It is increased to 0.35 s for the broadband excitation to get a longer signal in order to improve spectral resolution.

5.2. Harmonic excitation

5.2.1. Effect of the incident SPL

Results are first considered for several incident SPL and for a driving frequency of 1600 Hz, which is close to the resonant frequency of the liner. The contours of the SPL are depicted in Fig. 21 for four incident SPL. The reference for the SPL calculation is chosen here as the rms amplitude of the incident wave to ease the comparison between the results. The SPL maps are globally similar in the rigid section for $x < L_1$. For the incident SPL of 120 and 130 dB, differences from the case of an incident SPL equal to 80 dB can already be seen. The isolines above the liner are noticeably modified, especially the slope on the liner. The SPL in the exit section ($x > L_2$) also depends on the incident SPL. Finally, for the largest incident SPL of 140 dB, strong alteration of the SPL map is observed.

In order to analyze the evolution of the acoustic field with the incident SPL, the properties of the liner are investigated. Fig. 22 shows the variation of the rms velocity in the perforations along the liner for three incident SPL of 120, 130 and 140 dB. The effect of the liner is reflected by the reduction of v_{rms} along the liner. It decreases almost linearly for the incident SPL of 130 and 140 dB. For 120 dB, it decreases also linearly at the beginning of the liner but less rapidly from $x = 0.4 \text{ m}$.

The corresponding spatial variation of the surface impedance is depicted in Fig. 23 for four incident SPL. For the smallest incident SPL (80 dB), the real and imaginary parts of the impedance are constant along the liner and equal to the values in the linear regime.

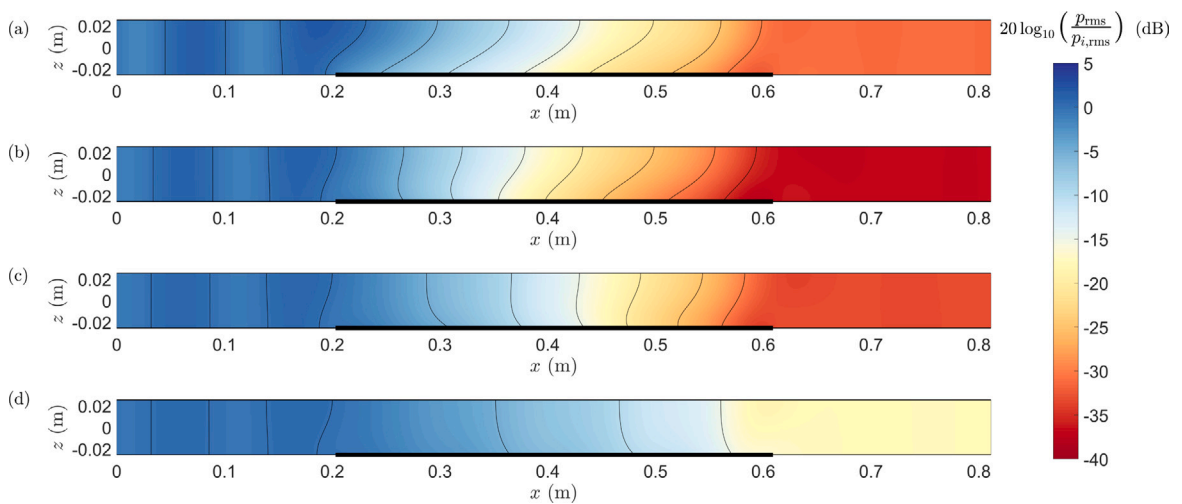


Fig. 21. SPL ($20 \log_{10}(p_{rms}/p_{i,rms})$) in dB for an incident SPL of: (a) 80 dB, (b) 120 dB, (c) 130 dB and (d) 140 dB with a harmonic excitation at $f = 1600$ Hz. The liner location is indicated by the black thick horizontal line. Isolines are plotted every 5 dB in black lines.

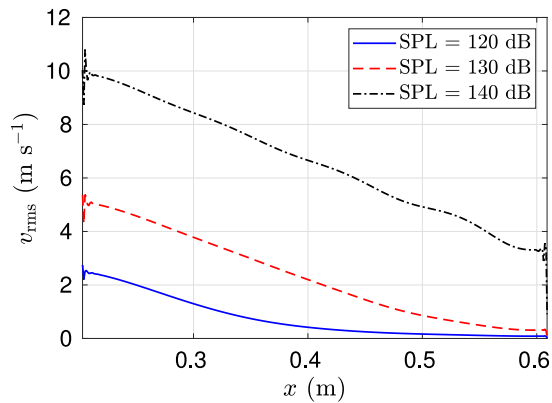


Fig. 22. Variation along the liner of the rms velocity for three incident SPL of 120, 130 and 140 dB with a harmonic excitation at $f = 1600$ Hz.

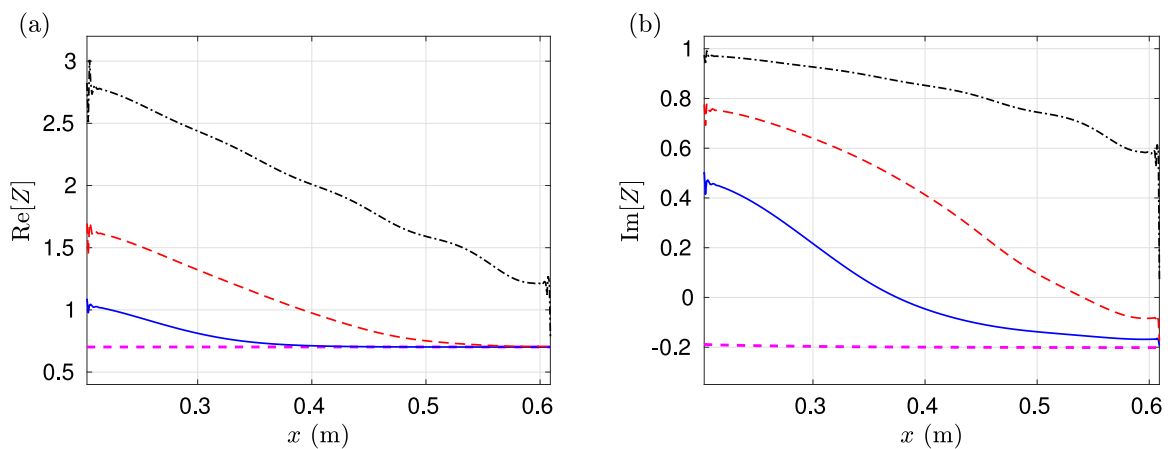


Fig. 23. Variation along the liner of the real (a) and imaginary (b) parts of the impedance for four incident SPL of 80 dB (magenta dashed lines), 120 dB (blue solid lines), 130 dB (red dashed lines) and 140 dB (black dashed-dotted lines) with a harmonic excitation at $f = 1600$ Hz. (For interpretation of the references to color in this figure legend, the reader is referred to the web version of this article.)

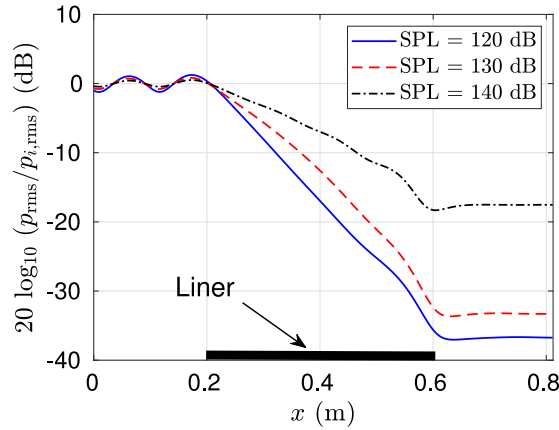


Fig. 24. Variation along the wall opposite to the liner of the SPL for three incident SPL of 120, 130 and 140 dB with a harmonic excitation at $f = 1600$ Hz.

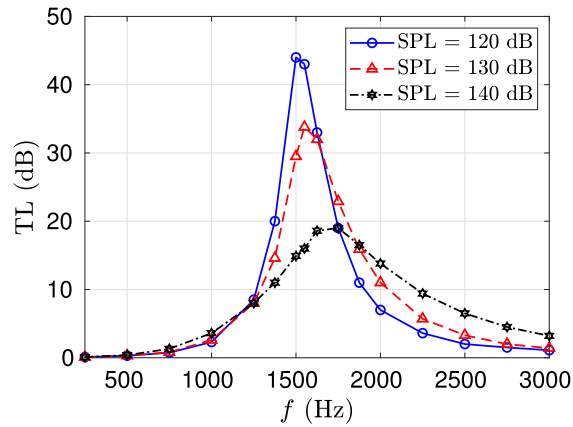


Fig. 25. Transmission loss versus frequency for a harmonic excitation with incident SPL of 120, 130 and 140 dB.

As the SPL increases, large spatial variations of the impedance are noticed. In more details, the impedance is seen to vary at the beginning of the liner before reaching almost the impedance value in the linear regime. Thus, the resistance is almost equal to that in the linear regime from $x = 0.4$ m for an incident SPL of 120 dB and from $x = 0.55$ m for an incident SPL of 130 dB. For the largest SPL (140 dB), this is however not the case and the impedance remains different from that in the linear regime along the whole liner. The spatial variations of the impedance echo the recent studies of Lafont et al. [40] and Chen et al. [41], in which impedance eduction of PP liners in high SPL environments was performed from measurements or numerical simulations. In order to improve comparisons with the reference results, a spatially-varying impedance function (linear or piecewise linear) was used. This was also discussed in detail by Roncen et al. [16]. The authors proposed an iterative strategy based on a frequency-domain solver of the linearized Euler equations for two objectives: first, for prediction of the acoustic field in a duct lined with a perforate plane liner accounting for the spatial variations of the surface impedance and second, for eduction of a spatially-varying surface impedance at high excitation level from measurements.

The evolution of the SPL along the wall opposite to the liner is plotted in Fig. 24 for three incident SPL. It is seen that the SPL varies in a similar manner for the three incident SPL: it is approximately constant in the rigid sections and decreases almost linearly in the lined section. The attenuation due to the liner however depends significantly on the incident SPL: it is quite similar for incident SPL of 120 dB and 130 dB, with a value of 36 dB and 33 dB, respectively, but suffers a dramatic reduction to 18 dB for an incident SPL of 140 dB.

In order to characterize the variation of the attenuation with the driving frequency, the transmission loss (TL) is determined from the numerical solution. The plane wave mode is the only propagating mode in the rigid sections, as the driving frequencies are below the duct cutoff frequency. Thus, the transmission loss can be calculated with:

$$TL = 20 \log_{10} \left(\frac{p_{t,rms}}{p_{i,rms}} \right) \quad (30)$$

where $p_{t,rms}$ is the rms value of the transmitted wave amplitude in the exit section. As an anechoic termination is considered, $p_{t,rms}$ is simply calculated from the acoustic pressure at a point sufficiently far from the liner. The transmission loss is shown for three

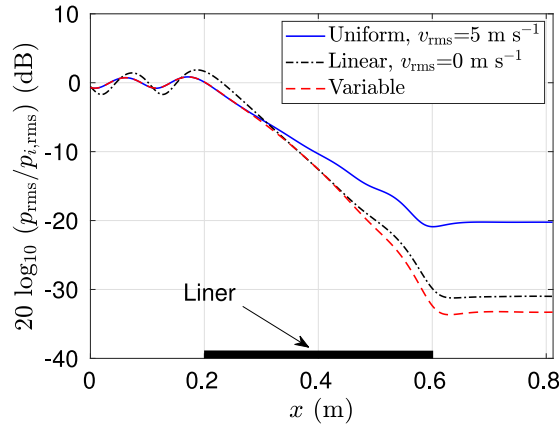


Fig. 26. Variation along the wall opposite to the liner of the SPL for an incident SPL of 130 dB with a harmonic excitation at $f = 1600$ Hz: spatially variable admittance (red dashed line), linear admittance (black dashed-dotted line) and spatially uniform admittance with $v_{\text{rms}} = 5 \text{ m s}^{-1}$ (blue solid line).

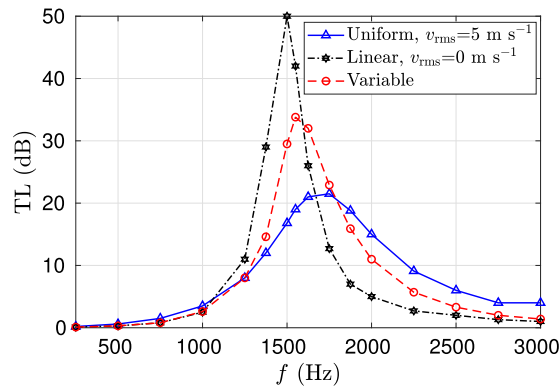


Fig. 27. Comparison of the transmission loss for an incident SPL of 130 dB between three cases: spatially variable admittance (red), linear admittance (black) and spatially uniform admittance with $v_{\text{rms}} = 5 \text{ m s}^{-1}$ (blue).

incident SPL in Fig. 25. It is seen that increasing the incident SPL tends to widen the TL peak and reduce its amplitude. The TL peak is observed near the resonant frequency of the liner and is shifted towards higher frequencies with the increase of the incident SPL. Note that the TL peak is not at the resonant frequency of the liner because the optimal impedance at grazing incidence and for a liner of finite length is not equal to that at normal incidence.

5.2.2. Influence of the impedance spatial variation

An additional study is performed to investigate more precisely the influence of the impedance modeling on the prediction of sound propagation and attenuation in a lined duct under high level of excitation. To do so, three models of the liner are considered: first, the reference model with a spatially-varying nonlinear impedance model that accounts for the variation of v_{rms} along the liner, i.e. $Z_{\text{NL}}[\omega, v_{\text{rms}}(x)]$, second, a uniform impedance model using the nonlinear impedance model but for a constant and representative value of v_{rms} and third, the linear impedance model. Simulations are performed for an incident SPL of 130 dB.

The SPL variation along the wall opposite to the liner is depicted in Fig. 26 for a frequency of 1600 Hz and for the three liner models. Note that as the rms velocity in the perforations is about 5 m s^{-1} at the beginning in the liner for this frequency and for the incident SPL of 130 dB using the nonlinear impedance model (see Fig. 22), this value was chosen to determine the impedance in the uniform case. It is seen that the SPL prediction is significantly different for the three liner models. In particular, the SPL for a uniform impedance with $v_{\text{rms}} = 5 \text{ m s}^{-1}$ is superimposed with that for a spatially-varying impedance for $x < 0.3 \text{ m}$ but is then substantially smaller. The results for the linear model differ from those with the nonlinear model but a better estimation is obtained in the exit section than with the uniform case for this particular frequency and incident SPL.

Fig. 27 shows the transmission loss as a function of the frequency for the three liner models. The effect of the SPL on the transmission loss, shown in Fig. 25 discussed in Section 5.2.1, is here observed by comparing the TL between the linear and nonlinear impedance model: the TL peak is wider and shifted towards high frequencies and its amplitude is reduced for the nonlinear impedance model compared to the linear one. In addition, the TL determined for the spatially-varying impedance model and for the uniform impedance model dramatically differs; assuming a uniform impedance leads to an under-prediction of the TL peak amplitude and an over-prediction of the peak width and of the frequency at the peak.

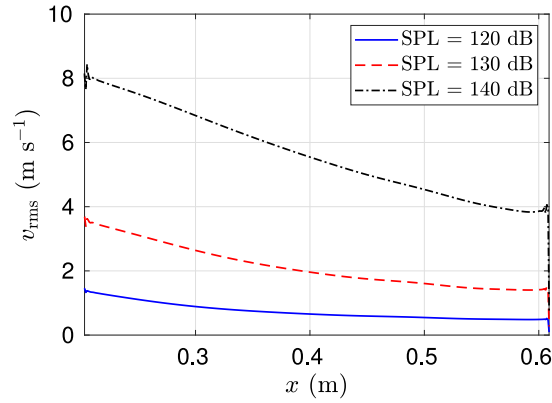


Fig. 28. Variation along the liner of the rms velocity for three incident SPL of 120, 130 and 140 dB with a broadband excitation.

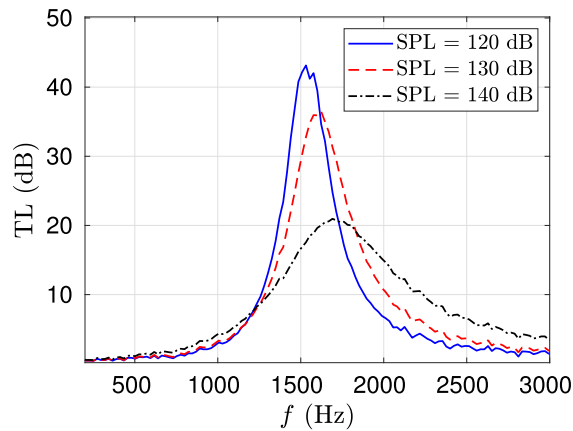


Fig. 29. Transmission loss versus frequency for a broadband excitation with incident SPL of 120, 130 and 140 dB.

Two conclusions can be drawn from this example. First, neglecting nonlinear effects on the response of a perforated plate can lead to a dramatic error on the prediction of the liner attenuation. Second, the spatial variations of the parameter governing the nonlinear effect on the liner impedance (here v_{rms}) should be taken into account for an accurate modeling of the liner acoustic properties and that assuming a constant value for the impedance at high SPL might be a rough approximation.

5.3. Broadband excitation

Finally, the case of an incident broadband signal is considered for different incident SPL.

The rms amplitude of the velocity in the perforations is plotted along the liner in Fig. 28. Compared to the harmonic excitation at $f = 1600$ Hz for the same incident SPL in Fig. 22, v_{rms} is in the same order of magnitude and similarly reduces along the liner. However, it decreases at a lower rate and its value at the beginning of the liner is smaller. For this given liner length, v_{rms} for the broadband excitation is thus smaller than that for the harmonic excitation in the first part of the lined section and larger in the second part.

Fig. 29 shows the transmission loss in the case of the broadband signal. It is determined with:

$$\text{TL} = 10 \log_{10} \left(\frac{S_{ii}}{S_{tt}} \right) \quad (31)$$

where S_{ii} and S_{tt} are the power spectral densities of the incident and transmitted pressure signal, respectively. The evolution of the TL for the broadband excitation is similar to that observed for the harmonic excitation in Fig. 25. Actually, the TL for PP#1 and for the three incident SPL are, remarkably, almost identical for both types of excitation: thus, the width and amplitude of the TL peak is similar and it is observed near the same frequencies. While this should be the case in the linear regime, it is seen that, for this particular liner, the liner attenuation does not depend significantly on the type of excitation. Some differences in the TL can however be noticed. For example, the TL at $f = 1600$ Hz for an incident SPL of 130 dB is equal to 32 dB for a harmonic excitation but to 36 dB for the broadband excitation. In addition, the maximum of TL is observed near a frequency of 1600 Hz for the broadband excitation but near 1550 Hz for a harmonic excitation.

A thorough analysis of the difference in the acoustic propagation along a lined duct depending on the type of excitation remains to be done and can be the subject of future research.

6. Conclusion

Time-domain admittance boundary conditions in the nonlinear regime were investigated to model the acoustic behavior of liners under a high excitation level. A particular focus was brought on perforated plate liners. The nonlinear model of Laly et al. [12] was employed for that. It accounts for the variation of the surface admittance with the frequency and the rms velocity in the perforation.

Two extensions of the TDABC proposed by Troian et al. [24] in the linear regime were considered. They are both based on a multipole model, so that the TDABC can be evaluated by integrating ODEs. The variation of the surface admittance with the rms velocity is dealt with by interpolation from a set of reference values. They however differ on the interpolation process. The first nonlinear TDABC, referred to as the IA method and proposed by Shur et al. [26], is based on the direct interpolation of the admittance. The IA method thus requires to determine a multipole approximation of the surface admittance model for each reference value; the number of poles of the corresponding nonlinear multipole model is therefore considerably larger than the linear counterpart. In the second nonlinear TDABC, called the IAP method, interpolation of the multipole function coefficients is preferred. This allows for a large reduction in the number of poles compared to the IA method.

The two methods were implemented in a finite-difference time-domain solver of the linearized Euler equations. Numerical experiments and comparisons with measurements on an impedance tube configuration were performed for validation and evaluation purposes. Three PP liners were considered for a harmonic and a broadband excitation. It was shown that the IA and IAP methods allow both for an accurate and efficient representation of the surface admittance in the nonlinear regime. Depending on the situation, one of the two methods is preferable. When considering analytical models for which the admittance varies smoothly with the frequency, a multipole function with only two poles is sufficient to accurately represent the admittance. Since the IAP has the smallest computational cost (because of the smallest number of poles), it may be preferred over the IA method in this case. When considering experimental admittance data, the multipole representation may require a significantly larger (5 to 8) number of poles in order to achieve acceptable accuracy. With such number of poles, the IAP approach may well become inaccurate because of the high sensitivity of the multipole function to the location of the poles and may lead to non-physical results, such a negative resistance over a given frequency band. Furthermore, the admittance approximation with a decent accuracy may require using different number of poles for different reference values of v_{rms} ; this is not possible with the current formulation of the IAP method. For such cases, the IA method may be superior.

Finally, the proposed TDABC was applied to sound propagation along a 2D lined duct under high level of excitation. It was exemplified that the spatial variations of the surface impedance are significant near the resonant frequency of the liner and has to be taken into account for an accurate prediction of liner attenuation at high SPL.

There are several ways to pursue this study. The simulations have been restricted to a medium at rest. Future work will consider the effect of a mean flow. Besides, along impedance tube measurements, it will be interesting to have a detailed acoustic database on a duct lined with a PP absorber for benchmarking. In addition, the concept of optimal impedance has been developed for a lined duct with a uniform impedance. It should be extended to the case of a spatially-varying impedance to be applicable to perforated liners at high level of excitation. Finally, a methodology to account for extended-reacting liners in time-domain simulations has been recently proposed in Alomar et al. [42]. In particular, perforated liners with a back cavity were considered by modeling the perforated plate by an impedance jump. Following the nonlinear TDABC investigated in this paper, it would be also possible to extend this methodology for perforated liners in the nonlinear regime.

CRedit authorship contribution statement

Daher Diab: Conceptualization, Methodology, Validation, Experiments, Investigation, Writing – original draft, Writing – review & editing. **Didier Dragna:** Conceptualization, Methodology, Writing – original draft, Formal analysis. **Edouard Salze:** Conceptualization, Methodology, Validation, Experiments, Investigation. **Marie-Annick Galland:** Conceptualization, Methodology, Writing – review & editing, Supervision, Funding acquisition.

Declaration of competing interest

The authors declare that they have no known competing financial interests or personal relationships that could have appeared to influence the work reported in this paper.

Acknowledgments

This work was performed within the framework of the Labex CeLyA of the University of Lyon, within the program “Investissements d’Avenir” (ANR-10-LABX-0060/ANR-16-IDEX-0005) operated by the French National Research Agency. This project has received funding from the Clean Sky 2 Joint Undertaking under the European Union’s Horizon 2020 research and innovation program under grant agreement N° 821093 (SALUTE). This publication reflects only the author’s view and the JU is not responsible for any use that may be made of the information it contains.

Table A.4
Poles and coefficients of the multipole model for the interpolation of the admittance (IA) method.

PP#1, Cavity depth of 10 mm						
Reference rms velocity (m s ⁻¹)	2	4	6	8	10	12
Re[A ₁]	1.680e+03	1.840e+03	1.962e+03	2.035e+03	2.085e+03	2.129e+03
Im[A ₁]	2.827e+02	4.331e+02	6.624e+02	9.044e+02	1.162e+03	1.532e+03
Re[λ ₁] (s ⁻¹)	1.609e+03	2.504e+03	3.675e+03	4.770e+03	5.795e+03	7.029e+03
Im[λ ₁] (s ⁻¹)	-1.054e+04	-1.091e+04	-1.096e+04	-1.076e+04	-1.041e+04	-9.776e+03
Y _∞	4.0492e-03	1.7636e-03	7.288e-04	3.7514e-04	2.231e-04	1.315e-04
PP#1, Cavity depth of 30 mm						
Reference rms velocity (m s ⁻¹)	2	4	6	8	10	12
Re[A ₁]	1.552e+03	1.700e+03	1.803e+03	1.861e+03	1.900e+03	1.933e+03
Im[A ₁]	3.983e+02	6.782e+02	1.115e+03	1.675e+03	2.547e+03	6.661e+03
Re[λ ₁] (s ⁻¹)	1.418e+02	2.290e+03	3.369e+03	4.359e+03	5.280e+03	6.382e+03
Im[λ ₁] (s ⁻¹)	-5.771e+03	-5.792e+03	-5.460e+03	-4.849e+03	-3.940e+03	-1.852e+03
Y _∞	4.949e-03	1.723e-03	6.431e-04	3.223e-04	1.921e-04	1.154e-04

Table A.5
Constants of the rational functions used for the coefficients of the multipole model with the interpolation of the admittance parameters (IAP) method.

PP#1, Cavity depth of 10 mm					
X	Re[A ₁]	Im[A ₁]	Re[λ ₁] (s ⁻¹)	Im[λ ₁] (s ⁻¹)	Y _∞
a	1.430e+03	1.965e+02	9.911e+02	-9.678e+03	2.379e-04
b	5.176e+02	3.294e+01	3.717e+02	-1.054e+03	-5.229e-03
c	1.033e+02	9.665e+00	1.853e+02	4.519e+01	4.199e-02
d	2.746e-01	2.404e-02	2.785e-01	5.174e-02	5.924e-01
e	4.354e-02	9.060e-08	1.431e-03	3.785e-08	3.499e+00
PP#1, Cavity depth of 30 mm					
X	Re[A ₁]	Im[A ₁]	Re[λ ₁] (s ⁻¹)	Im[λ ₁] (s ⁻¹)	Y _∞
a	1.308e+03	1.738e+02	7.187e+02	-5.398e+03	1.310e-02
b	8.897e+02	8.252e+01	4.897e+02	1.402e+01	-1.615e-03
c	3.224e+02	-6.832e+00	2.652e+02	2.951e+01	7.271e-05
d	6.127e-01	-1.235e-01	4.883e-01	-3.844e-02	5.355e-02
e	1.517e-01	3.524e-03	8.734e-04	3.995e-09	2.183e-01

Appendix A. Coefficients of the nonlinear TDABC

This appendix provides the coefficients of the nonlinear TDABC for the PP#1 absorber with two cavity depths 10 and 30 mm. The Laly model for this liner is approximated by a single pair of complex conjugate poles λ_1 and $\lambda_2 = \lambda_1^*$, with $A_2 = A_1^*$ over the range of velocities in the perforations considered in this paper.

For the interpolation of the admittance (IA) method, the poles and the coefficients of the multipole model (see Eq. (13)) are given for the different reference values of the rms velocity in the perforations in Table A.4.

For the interpolation of the admittance parameters (IAP) method, the poles and the coefficients (see Eq. (22)) are approximated by a rational function with quadratic polynomials, that can be written as follows:

$$X(v_{\text{rms}}) = \frac{a + b v_{\text{rms}} + c v_{\text{rms}}^2}{1 + d v_{\text{rms}} + e v_{\text{rms}}^2}. \quad (\text{A.1})$$

The constants a , b , c , d and e are given for each coefficient of the multipole model in Table A.5.

Appendix B. Additional comparisons with impedance tube experiments for broadband excitation

In this appendix, additional comparisons between the impedance tube measurements for a broadband excitation and corresponding numerical results are presented. The experimental set-up is described in Section 4.3 and the procedure used for the numerical simulations is detailed in Section 4.3.2.

Fig. B.30 shows the surface admittance and the absorption coefficient for PP#2 with a cavity depth of 30 mm and for three incident sound pressure levels. The experimental results are qualitatively similar to those obtained for PP#1 in Figs. 18 and 19. The increase of the incident sound pressure level leads to a flattening of the admittance curves and a reduction and a broadening of the absorption peak. The results obtained with the numerical simulations do not match exactly the experimental curves, but the evolution of the admittance and the absorption coefficient with the incident SPL is correctly reproduced. Note also that the numerical results provide a close agreement with the analytical model.

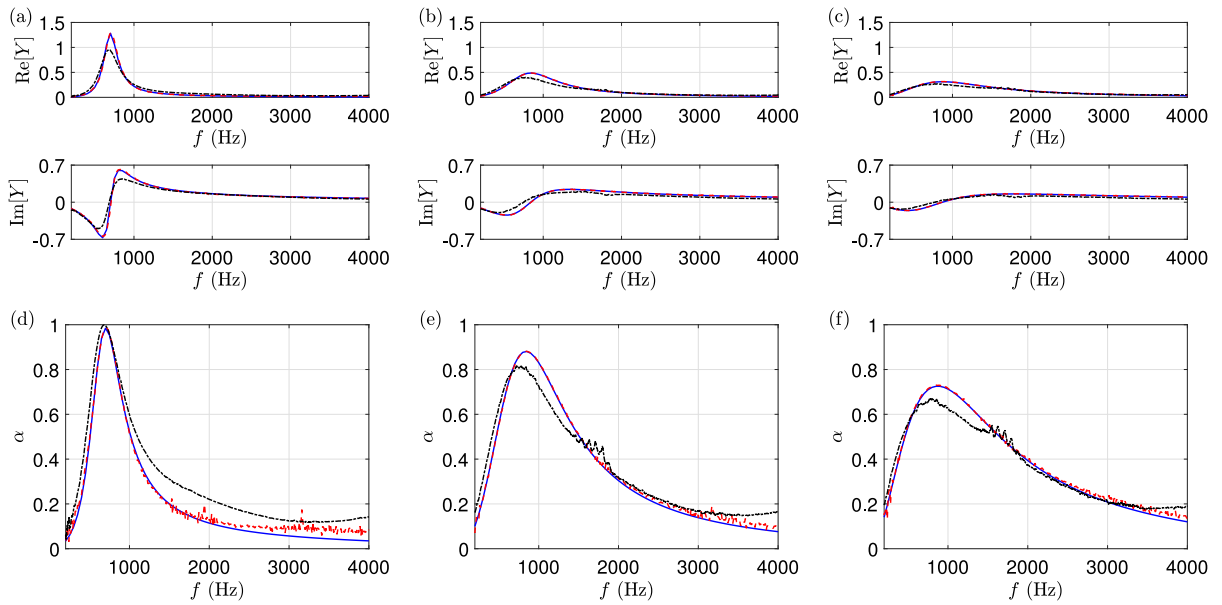


Fig. B.30. (top) Surface admittance and (bottom) absorption coefficient of PP#2 absorber with a cavity depth of 30 mm for a broadband excitation and for three incident SPL (a)–(d) 76.8 dB, (b)–(e) 126.5 dB and (c)–(f) 133.4 dB: measured (black dash-dotted) and determined from the analytical model in Eq. (3) (blue solid) and from the numerical solution (red dashed).

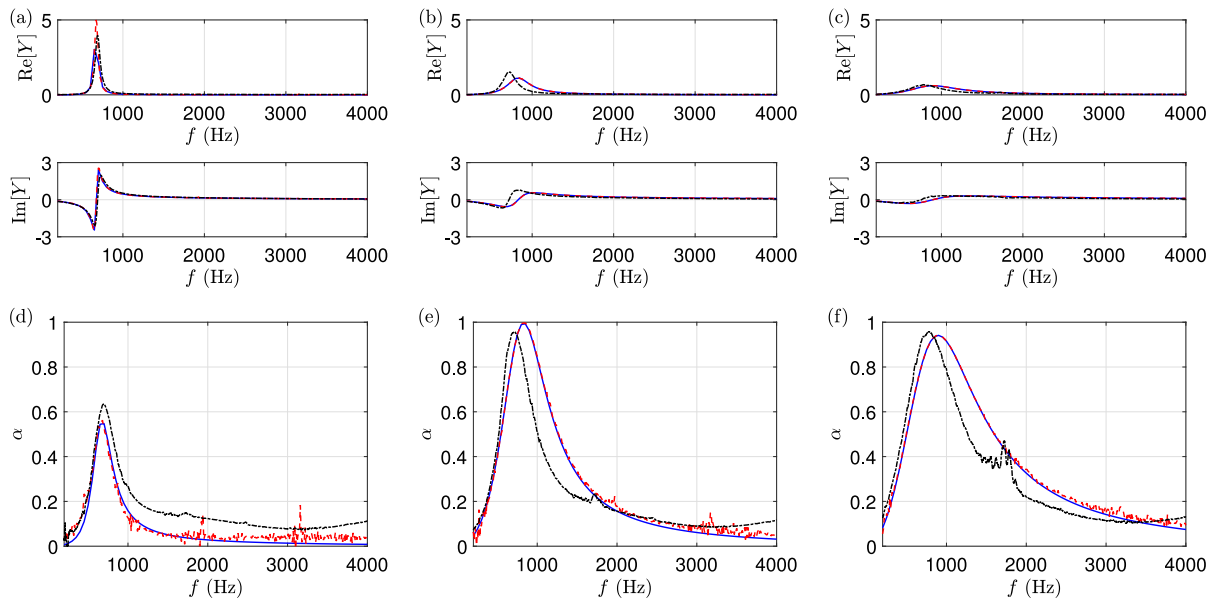


Fig. B.31. (top) Surface admittance and (bottom) absorption coefficient of PP#3 absorber with a cavity depth of 30 mm for a broadband excitation and for three incident SPL (a)–(d) 76.6 dB, (b)–(e) 125.3 dB and (c)–(f) 133.5 dB: measured (black dash-dotted) and determined from the analytical model in Eq. (3) (blue solid) and from the numerical solution (red dashed).

Corresponding results for PP#3 with a cavity depth of 30 mm are plotted in Fig. B.31. In this case also, the experimental admittance curves tends to flatten with the increase of the incident SPL. Nevertheless, the absorption coefficient behaves differently. The absorption coefficient significantly rises with the increase of the incident SPL from 76.6 dB to 125.3 dB. Then, the peak value decreases and the absorption peak broadens with a further increase of the incident SPL up to 133.5 dB. The numerical simulations predict the overall evolution of the admittance and the absorption coefficient with the increase of the incident SPL. Discrepancies are however noticeable for this PP absorber. For the incident SPL of 125.3 dB, the peak in $\text{Re}[Y]$ is thus predicted at a higher frequency. The absorption peak is also shifted towards high frequencies with the increase of the SPL, while it is centered around

Table B.6

Rms amplitude of the velocity in the perforations for PP#2 and PP#3 absorbers with a cavity depth of 30 mm for a broadband excitation: values deduced from the experiments and from the numerical simulations.

PP#2, Cavity depth of 30 mm								
Incident SPL (dB)		76.8	86.5	97.2	106.7	116.5	126.5	133.4
v_{rms} (m s ⁻¹)	exp.	1.59×10^{-2}	4.59×10^{-2}	1.56×10^{-1}	4.58×10^{-1}	1.35	3.78	7.13
	num.	1.93×10^{-2}	6.17×10^{-2}	2.16×10^{-1}	6.02×10^{-1}	1.60	4.03	7.16
PP#3, Cavity depth of 30 mm								
Incident SPL (dB)		76.6	86.6	96.4	106.2	116.1	125.3	133.5
v_{rms} (m s ⁻¹)	exp.	1.24×10^{-2}	3.73×10^{-2}	1.15×10^{-1}	3.55×10^{-1}	1.07	2.84	6.43
	num.	2.23×10^{-2}	7.34×10^{-2}	2.17×10^{-1}	6.19×10^{-1}	1.70	3.52	6.61

a frequency independent of the incident SPL in the experiments. In addition, the results from the analytical model and from the numerical simulations show a close agreement.

Finally, Table B.6 indicates the rms amplitude of the velocity in the perforations for PP#2 and PP#3 with a cavity depth of 30 mm determined from the measurements and from the numerical simulations. While a decent prediction is noticed, the value of v_{rms} tends to be overestimated in the numerical simulations, in particular in the linear regime. In the nonlinear regime, the differences between the values determined from the experiments and the numerical simulations reduce. Thus, v_{rms} is accurately predicted with an error smaller than 5% for the largest incident SPL.

Appendix C. Supplementary data

Supplementary material related to this article can be found online at <https://doi.org/10.1016/j.jsv.2022.116892>.

References

- [1] L. Sivian, Acoustic impedance of small orifices, *J. Acoust. Soc. Am.* 7 (1935) 94–101.
- [2] C.K.W. Tam, H. Ju, M.G. Jones, W.R. Watson, T.L. Parrott, A computational and experimental study of resonators in three dimensions, *J. Sound Vib.* 329 (2010) 5164–5193.
- [3] Q. Zhang, D.J. Bodony, Numerical investigation and modelling of acoustically excited flow through a circular orifice backed by a hexagonal cavity, *J. Fluid Mech.* 693 (2012) 367–401.
- [4] A.W. Guess, Calculation of perforated plate liner parameters from specified acoustic resistance and reactance, *J. Sound Vib.* 40 (1975) 119–137.
- [5] D.-Y. Maa, Potential of microperforated panel absorber, *J. Acoust. Soc. Am.* 104 (1998) 2861–2866.
- [6] A. Hersh, B. Walker, J. Celano, Helmholtz resonator impedance model, part 1: Nonlinear behavior, *AIAA J.* 41 (2003) 795–808.
- [7] H. Bodén, Y. Guo, H.B. Tözün, Experimental investigation of nonlinear acoustic properties for perforates, in: 12th AIAA/CEAS Aeroacoustics Conference, 27th AIAA Aeroacoustics Conference, Cambridge, MA, USA, 8–10 May, 2006, AIAA Paper 2006–2404, 2020, pp. 1–8.
- [8] R. Tayong, T. Dupont, P. Leclaire, On the variations of acoustic absorption peak with particle velocity in micro-perforated panels at high level of excitation, *J. Acoust. Soc. Am.* 127 (2010) 2875–2882.
- [9] S.-H. Park, A design method of micro-perforated panel absorber at high sound pressure environment in launcher fairings, *J. Sound Vib.* 332 (2013) 521–535.
- [10] U. Ingard, H. Ising, Acoustic nonlinearity of an orifice, *J. Acoust. Soc. Am.* 42 (1967) 6–17.
- [11] T.H. Melling, The acoustic impedance of perforates at medium and high sound pressure levels, *J. Sound Vib.* 29 (1973) 1–65.
- [12] Z. Laly, N. Atalla, S.-A. Meslioui, Acoustical modeling of micro-perforated panel at high sound pressure levels using equivalent fluid approach, *J. Sound Vib.* 427 (2018) 134–158.
- [13] N. Atalla, F. Sgard, Modeling of perforated plates and screens using rigid frame porous models, *J. Sound Vib.* 303 (2007) 195–208.
- [14] A. Cummings, Transient and multiple frequency sound transmission through perforated plates at high amplitude, *J. Acoust. Soc. Am.* 74 (1986) 942–951.
- [15] W. Eversman, Effect of local impedance variation and non-linearity on multiple tone attenuation, *Int. J. Aeroacoustics* 14 (2015) 281–303.
- [16] R. Roncen, F. Méry, E. Piot, P. Klotz, Spatially-varying impedance model for locally reacting acoustic liners at a high sound intensity, *J. Sound Vib.* 524 (116741) (2022) 1–19.
- [17] Y. Özyörük, L. Long, A time-domain implementation of surface acoustic impedance condition with and without flow, *J. Comput. Acoust.* 5 (1997) 277–296.
- [18] C.K.W. Tam, L. Auriault, Time-domain impedance boundary conditions for computational aeroacoustics, *AIAA J.* 34 (1996) 917–923.
- [19] K.Y. Fung, H. Ju, Broadband time-domain impedance models, *AIAA J.* 39 (2001) 1449–1454.
- [20] C. Richter, F.H. Thiele, X.D. Li, M. Zhuang, Comparison of time-domain impedance boundary conditions for lined duct flows, *AIAA J.* 45 (2007) 1933–1945.
- [21] F. Monteghetti, D. Matignon, E. Piot, L. Pascal, Design of broadband time-domain impedance boundary conditions using the oscillatory-diffusive representation of acoustical models, *J. Acoust. Soc. Am.* 140 (2016) 1663–1674.
- [22] Y. Reyren, M. Baelmans, W. Desmet, Efficient implementation of Tam and Auriault's time-domain impedance boundary condition, *AIAA J.* 46 (2008) 2368–2376.
- [23] X.Y. Li, X.D. Li, C.K.W. Tam, Improved multipole broadband time-domain impedance boundary condition, *AIAA J.* 50 (2012) 980–984.
- [24] R. Troian, D. Dagna, C. Bailly, M.-A. Galland, Broadband liner impedance eduction for multimodal acoustic propagation in the presence of a mean flow, *J. Sound Vib.* 392 (2017) 200–216.
- [25] D. Dagna, P. Pineau, P. Blanc-Benon, A generalized recursive convolution method for time-domain propagation in porous media, *J. Acoust. Soc. Am.* 138 (2015) 1030–1042.
- [26] M. Shur, M. Strelets, A. Travin, T. Suzuki, P. Spalart, Unsteady simulations of sound propagation in turbulent flow inside a lined duct, *AIAA J.* 59 (2021) 3054–3070.
- [27] J. Allard, N. Atalla, Propagation of Sound in Porous Media: Modelling Sound Absorbing Materials, second ed., John Wiley & Sons, 2009.
- [28] Z. Laly, N. Atalla, S.-A. Meslioui, K. El Bikri, Sensitivity analysis of micro-perforated panel absorber models at high sound pressure levels, *Appl. Acoust.* 156 (2019) 7–20.

- [29] C. Bogey, C. Bailly, A family of low dispersive and low dissipative explicit schemes for flow and noise computations, *J. Comput. Phys.* 194 (2004) 194–214.
- [30] J. Berland, C. Bogey, O. Marsden, C. Bailly, High-order, low dispersive and low dissipative explicit schemes for multiple-scale and boundary problems, *J. Comput. Phys.* 224 (2007) 637–662.
- [31] J. Berland, C. Bogey, C. Bailly, Low-dissipation and low-dispersion fourth-order Runge–Kutta algorithm, *Comput. & Fluids* 35 (2006) 1459–1463.
- [32] C. Bogey, N. De Cacqueray, C. Bailly, A shock-capturing methodology based on adaptative spatial filtering for high-order non-linear computations, *J. Comput. Phys.* 228 (2009) 1447–1465.
- [33] F. Monteghetti, D. Matignon, E. Piot, Energy analysis and discretization of nonlinear impedance boundary conditions for the time-domain linearized Euler equations, *J. Comput. Phys.* 375 (2018) 393–426.
- [34] B. Gustavsen, A. Semlyen, Rational approximation of frequency domain responses by vector fitting, *IEEE Trans. Power Deliv.* 14 (1999) 1052–1061.
- [35] R. Billard, Study of Perforated Liners for Aeronautics (Ph.D. thesis), Le Mans Université, 2021.
- [36] K.U. Ingard, *Theoretical Acoustics*, McGraw Hill, 1968.
- [37] J. Chung, D. Blaser, Transfer function method of measuring in-duct acoustic properties. I. Theory, *J. Acoust. Soc. Am.* 68 (1980) 907–913.
- [38] B.S. Beck, N.H. Schiller, M.G. Jones, Impedance assessment of a dual-resonance acoustic liner, *Appl. Acoust.* 93 (2015) 15–22.
- [39] M.G. Jones, W.R. Watson, T.L. Parrott, Benchmark data for evaluation of aeroacoustic propagation codes with grazing flow, in: 11th AIAA/CEAS Aeroacoustics Conference, Monterey, CA, USA, 23–25 May, 2005, AIAA Paper 2005–2853, pp. 1–18.
- [40] V. Lafont, F. Méry, R. Roncen, F. Simon, E. Piot, Liner impedance eduction under shear grazing flow at a high sound pressure level, *AIAA J.* 58 (2020) 1107–1117.
- [41] C. Chen, X. Li, F. Hu, On spatially varying acoustic impedance due to high sound intensity decay in a lined duct, *J. Sound Vib.* 483 (115430) (2020) 1–28.
- [42] A. Alomar, D. Dragna, M.-A. Galland, Time-domain simulations of sound propagation in a flow duct with extended-reacting liners, *J. Sound Vib.* 507 (116137) (2021) 1–24.